Weak and tunable adhesion-clutch drives rapid cell migration and glioblastoma motility

Kentarou Baba[1], Ami Fukushi-Kumagaya[1], Megumi Morisaki[1], Ryosuke Takeuchi[1], Zhize Xiao[2], Yoshikazu Nagashima[1], Mizuki Sakai[1], Yasuna Higashiguchi[1], Hiroko Katsuno-Kambe[1], Asako Katsuma[3], Yoshihiro Ueda[4], Yuji Kamioka[4], Daisuke Kawauchi[2], Tatsuo Kinashi[4], Yonehiro Kanemura[3,5], Naoyuki Inagaki[1,6,*]

[1]Division of Biological Science, Nara Institute of Science and Technology, Ikoma, Japan
[2]Department of Neuro-Oncology, Institute of Brain Science, Nagoya City University, Nagoya, Japan
[3]Division of Regenerative Medicine, Department of Biomedical Research and Innovation, Institute for Clinical Research, NHO Osaka National Hospital, Osaka, Japan
[4]Department of Molecular Genetics, Institute of Biomedical Science, Kansai Medical University, Hirakata, Japan
[5]Department of Neurosurgery, NHO Osaka National Hospital, Osaka, Japan
[6]Lead contact
*Correspondence: ninagaki@bs.naist.jp

SUMMARY

To move forward, migrating cells must exert backward forces against the extracellular environment. Recent studies have highlighted the importance of integrin-independent forces for cell migration; but the molecular machinery that exerts forces remains unclear. Here, we show that the clutch-linker molecule shootin1 and the cell adhesion molecule L1 transmit the backward force of treadmilling actin filaments to the adhesive environment for rapid dendritic cell migration. Notably, shootin1 and L1 transmit weak traction forces, ~100 times weaker than integrin-based forces, by constituting an integrin-independent slippery adhesion-clutch. This adhesion-clutch system is tunable in response to the chemoattractant CCL19 and the adhesive ligand laminin and mediates chemotaxis through its polarized activation within cells. Furthermore, its aberrant activity enhances glioblastoma cell motility. Our results show that the weak adhesion-clutch is well-suited for rapid cell migration, without forming strong adhesions that impede cell motility, and provides a potential target for inhibiting abnormal cell motility.

KEYWORDS

Migration, Chemotaxis, Haptokinesis, Cancer invasion, Leukocyte, Glioblastoma, Adhesion, Clutch, Traction force, Shootin1b

INTRODUCTION

Cell migration is essential for various biological processes, including immune response, development and regeneration, and requires bidirectional interactions with the extracellular environment. Namely, migrating cells must exert backward forces onto the environment to propel themselves forward; conversely, their speed and direction are regulated in response to various extracellular cues. Dysregulation of these interactions leads to pathogenesis such as cancer cell invasion. Intracellular actin filaments (F-actins) polymerize at the front of migrating cells and disassemble proximally, thereby undergoing backward flow (treadmilling)[1,2]. To explain the force to drive cell migration, the adhesion-clutch model was proposed[3,4]. In this model, clutch-linker molecules (e.g., talin and vinculin) and cell adhesion molecules (e.g., integrins) transmit the movement of F-actin flow to the adhesive environment, thereby exerting backward traction forces that drive cell migration.

Indeed, integrins and the linker molecules, including talin and vinculin, mediate mechanical coupling between F-actin flow and adhesive substrates[5-7], thereby generating large traction forces that can reach hundreds or kilo Pa[8,9]. However, KO of integrin, talin or vinculin does not always delay three-dimensional (3D) ameboid and two-dimensional (2D) mesenchymal migrations[6,7,10-13]. In contrast to the adhesion-clutch paradigm, integrin activation inhibits T cell motility[10] and inhibition of the integrin-mediated force transmission by vinculin depletion promotes fibroblast migration[7], highlighting a role of integrin-independent mechanisms[11,14,15]. Several alternative models have been proposed to explain the backward force exertion, including friction-based[15-19] and molecular paddling-based[20] mechanisms. In order to validate the force-exerting models, it is essential to identify the molecules that exert forces and to determine their mechanical dynamics. Thus, despite decades of intensive research, the mechanistic understanding of cell migration remains limited. In addition, it remains unclear how environmental chemical cues direct cell migration through force control[15,21,22].

Leukocytes undergo rapid ameboid cell migration in tissues; their velocities are up to ~100 times faster than those of mesenchymal and epithelial cells[11,23]. On the other hand, glioblastoma is the most common and most lethal primary brain tumor in adults with high invasiveness[24,25]. Shootin1a (*SHTN1*) is a neuronal clutch-linker molecule that transmit the force of F-actin flow to the environment for axonal extension[26-28] and

68 synaptic expansion[29]. We previously reported that shootin1b, a splicing variant of
69 shootin1a, is expressed in the leukocytes, dendritic cells[30]. The present study shows that
70 shootin1b and the cell adhesion molecule L1 form a tunable adhesion-clutch that
71 transmits weak backward forces at levels of 10 Pa and controls the speed and direction of
72 rapid dendritic cell migration under chemical cues. In addition, an aberrant expression of
73 shootin1b in glioblastoma cells promotes their abnormal migration by mediating the weak
74 adhesion-clutch. These results demonstrate that the weak adhesion-clutch enables rapid
75 cell migration and guidance by chemoattractants, and represents a potential target for
76 inhibiting glioblastoma invasion.
77
78 **RESULTS**
79 **Weak backward forces propel rapid dendritic cell migration**
80 To investigate the force that propels cell migration, we first monitored the forces
81 generated by migrating dendritic cells using traction force microscopy[31]. Mouse bone
82 marrow-derived dendritic cells in a mixture of collagen gel and Matrigel were plated on
83 laminin-coated polyacrylamide gels with embedded 200-nm fluorescent beads (Figure
84 1A). Dendritic cells express L1[32], and Matrigel contains its adhesion ligands laminins[33,34]
85 which are expressed in the dendritic cell migration pathways[35,36]. Consistent with the
86 previous reports[16,37], dendritic cells underwent rapid random migration in the presence of
87 20-200 ng/mL (2.1-21 nM) CCL19 under the semi-3D condition. Traction forces were
88 monitored by force-induced deformation of the polyacrylamide gel, visualized by the
89 bead movement (Video S1, Figure 1B). The cellular front of migrating dendritic cells
90 exerted prominent backward forces on the gel (yellow arrows, Video S1). We also
91 observed centripetal forces at the trailing region (yellow arrows). These data are
92 consistent with the forces generated by migrating dendritic cells detected by micropost
93 arrays in a 2D condition[38].
94 The force vectors detected by individual beads under a cell were averaged and
95 expressed as a single vector composed of magnitude and angle (θ)[31]. Dendritic cells
96 generated traction force of 8.8 ± 0.8 Pascal (Pa, pN/μm^2) in the presence of 20 ng/mL
97 CCL19 (Figure 1C). Increasing the CCL19 concentration to 200 ng/mL resulted in a
98 significant increase in the force, reaching 15.4 ± 0.4 Pa (Figure 1C). The amplitude of the
99 force generated by dendritic cells is very weak compared to the traction force produced

100 by focal adhesions (FAs), which can reach hundreds or kilo Pa[8,9]. Importantly, increasing
101 the CCL19 concentration from 20 ng/mL to 200 ng/mL also accelerated random dendritic
102 cell migration under 3D conditions (collagen gel + Matrigel) from 2.4 ± 0.1 μm/min to
103 3.2 ± 0.1 μm/min (Figures S1A-C, 1D, Video S2). Furthermore, a significant positive
104 correlation was observed between the angle of cell migration and the angle of traction
105 force + 180° (Figure 1E). We therefore conclude that the observed weak backward force
106 propels rapid dendritic cell migration.
107
108 **Shootin1b transmits forces for dendritic cell migration under CCL19 signaling**
109 We previously reported that dendritic cells express shootin1b, a splicing variant of
110 shootin1a (Figure S2A-B)[30]. Shootin1a is a neuronal clutch-linker molecule that mediates
111 actin-substrate coupling for axonal extension, through its interaction with the F-actin
112 binding protein cortactin and L1[27,28]. Stimulated emission depletion (STED) microscopy
113 demonstrated that shootin1b colocalizes with F-actins, cortactin, and L1 at the leading
114 edge (Figures 1F, S2C-D). To examine whether shootin1b is involved in the generation
115 of the traction force for dendritic cell migration, we analyzed dendritic cells prepared
116 from shootin1b knockout (KO) mice (Figure S2E-F). Shootin1b KO had no effect on the
117 traction force produced by dendritic cells in the presence of 20 ng/mL CCL19 (Figure
118 1C). On the other hand, shootin1b KO resulted in 48.6% inhibition of the increase in
119 traction force induced by 200 ng/mL CCL19 (Video S3, Figure 1C, G, H). Expression of
120 a shootin1 dominant-negative mutant (shootin1-DN), which disrupts the interaction
121 between endogenous shootin1 and L1[39], resulted in a similar reduction in the traction
122 force (Video S4, Figure S3A-C).
123 Consistently, although shootin1b KO did not affect the migration speed of
124 dendritic cells in the presence of 20 ng/mL CCL19 (Figures S1E, 1D), it led to 48.1%
125 inhibition of the migration speed increased by 200 ng/mL CCL19 (Video S5, Figures S1F,
126 1D, I). Together, these data indicate that shootin1b promotes forces for dendritic cell
127 migration under CCL19 signaling thorough its interaction with L1. In addition, the
128 parallel correlations between the reductions in traction forces and migration speeds
129 support our conclusion that the weak force drives dendritic cell migration.
130
131 **Shootin1b and L1 form a weak and slippery adhesion-clutch enhanced by laminin**

132 To analyze how shootin1b transmits weak forces on the substrate through L1, we
133 monitored their dynamics at the leading edge of dendritic cells. HaloTag-actin, HaloTag-
134 shootin1b or L1-HaloTag expressed in dendritic cells on the glass bottom dishes, coated
135 with the nonspecific adhesive substrate poly-D-lysine (PDL) or subsequently coated with
136 PDL and the extracellular matrix (ECL) protein laminin, were observed by speckle
137 imaging using total internal reflection fluorescence (TIRF) microscopy[31] in the presence
138 of 200 ng/mL CCL19. F-actins underwent backward movement at the leading edge of
139 dendritic cells (Video S6, Figure 2A) as reported[40]; shootin1b and L1 also moved
140 retrogradely (Video S6, Figure 2B-C). The velocities of F-actins, shootin1b, and L1 were
141 analyzed by tracing the speckles of HaloTag-actin, HaloTag-shootin1b and L1-HaloTag,
142 respectively (yellow lines, Figure 2A-C). Notably, F-actins, shootin1b and L1 moved at
143 similar rates of 1.7 ± 0.1 μm/min, 1.8 ± 0.1 μm/min and 1.8 ± 0.1 μm/min, respectively,
144 on laminin (Figure 2D), suggesting that shootin1b and L1 move by stably interacting with
145 F-actins (Figure 2E) in the presence of 200 ng/mL CCL19. On the other hand, F-actins,
146 shootin1b and L1 showed a similar increase in velocity in the absence of laminin (Video
147 S6, Figure 2D, F-H). Thus, shootin1b and L1 form a weak adhesion-clutch that
148 continuously slips on the adhesive substrate, in which the L1-substrate interphase is
149 enhanced by laminin (Figure 2E).
150
151 **Shootin1b-mediated adhesion-clutch is highly sensitive to CCL19**
152 Stimulation of the CCL19 receptor CCR7 activates Cdc42 and Rac1 and their
153 downstream kinase Pak1[41,42], which are required for CCL19-induced dendritic cell
154 chemotaxis[37,42]. Pak1 phosphorylates shootin1a at Ser101 and Ser249 in neurons[43], which
155 in turn enhances adhesion-clutch by promoting shootin1a-cortactin and shootin1a-L1
156 interactions[28,39]; shootin1b also contains Ser101 and Ser249[30]. To investigate how
157 shootin1b promotes dendritic cell migration under CCL19 signaling, we examined
158 shootin1b phosphorylation in dendritic cells. In the absence of CCL19, low levels of
159 shootin1b phosphorylations at Ser101 and Ser249 were detected (Figure 3A). The
160 phosphorylations increased markedly in a dose- and time-dependent manner, reaching
161 saturation at 200 ng/mL CCL19 (Figure 3A-B) and 10 min (Figure S4A-B), respectively.
162 They were inhibited by the Pak1 inhibitor NVS-PAK1-1 (Figure S4C-D), indicating that
163 CCL19 triggers Pak1-mediated shootin1b phosphorylation in dendritic cells. Furthermore,

164 immunoprecipitation analyses showed that the amounts of L1 and cortactin co-
165 precipitated with shootin1b were strongly increased by increasing the concentration of
166 CCL19 concentration from 0 ng/mL to 200 ng/mL (Figure 3C-D), indicating that the
167 shootin1b-L1 and shootin1b-cortactin interactions are highly sensitive to CCL19
168 concentration.

169 We further monitored the adhesion-clutch dynamics under CCL19 stimulation.
170 Dendritic cells were transfected with HaloTag-actin and Lifeact-EGFP and cultured on
171 laminin-coated dishes for observation (Video S7, Figure 3E). F-actin flow velocity was
172 analyzed by tracing the speckles of HaloTag-actin (magenta double-headed arrow, Figure
173 3E), while actin polymerization rate was calculated as the sum (blue double-headed
174 arrow) of F-actin protrusion rate monitored by Lifeact-EGFP (green double-headed
175 arrow) and the F-actin flow velocity (magenta double-headed arrow)[31]. Actin
176 polymerization rate increased with an increase in CCL19 concentration from 20 ng/mL
177 to 200 ng/mL (yellow asterisks in Figure 3F), consistent with a previous report using T
178 cells[16].

179 Importantly, despite the increased actin polymerization, F-actin flow velocity
180 decreased by 200 ng/mL CCL19 (green asterisks in Figure 3G). The decreased F-actin
181 flow velocity and the increased traction force (Figure 1C) are the key indicators of
182 increased adhesion-clutch[6,7,43]. In shootin1b KO dendritic cells, the increase in CCL19
183 concentration from 20 ng/mL to 200 ng/mL increased the F-actin flow velocity (blue
184 asterisk in Figure 3G), indicating that CCL19 enhances shootin1b-mediated adhesion-
185 clutch. On the other hand, shootin1b KO did not affect the increased actin polymerization
186 induced by 200 ng/mL CCL19 (blue n.s., Figure 3F). Thus, CCL19 signaling leads to a
187 dual enhancement of shootin1b-mediated adhesion-clutch and actin polymerization at the
188 leading edge (Figure 3H).

189

190 **Shootin1b drives CCL19-induced chemotaxis through polarized activation**

191 Dendritic cells migrate under CCL19 gradients *in vivo* from various tissues, including the
192 skin, to lymph nodes through lymphatic vessels[44-46]. Next, we analyzed dendritic cell
193 chemotaxis in 3D conditions (collagen gel + Matrigel) under CCL19 gradients. Dendritic
194 cells underwent chemotaxis toward the CCL19 source (Video S8, Figure 4A) as
195 reported[47]; on the other hand, shootin1b KO partially inhibited dendritic cell migration

196 toward the CCL19 source (Video S8, Figure 4B). To further analyze the effects of
197 shootin1b KO, we calculated the chemotaxis index (straight distance toward the CCL19
198 source/total distance) by tracing the migration trajectories (Figure 4C). The mean
199 migration speed and chemotaxis index of control dendritic cells were 4.4 ± 0.2 μm/min
200 and 0.5 ± 0.02, respectively (blue dots, Figure 4D-E). Deletion of shootin1b not only
201 reduced the migration speed (red dots, Figure 4D), but also decreased the chemotaxis
202 index (red dots, Figure 4E). Similarly, expression of shootin1-DN reduced the migration
203 speed and chemotaxis index (Video S8, Figure S5). Together, these data indicate that the
204 shootin1b- and L1-mediated adhesion-clutch drives CCL19-induced dendritic cell
205 chemotaxis.

206 We further examined shootin1b activation under a CCL19 gradient. A CCL19
207 gradient was applied to dendritic cells expressing myc-shootin1b for 30 min. They were
208 then fixed and immunolabeled with an antibody that recognizes shootin1b
209 phosphorylation at Ser249 (red, Figure 4F). Localization of shootin1b (phosphorylated
210 and unphosphorylated shootin1b) was visualized with an anti-myc antibody (blue). As
211 shown in Figure 4F, polarized localization of the phosphor-shootin1b was observed within
212 dendritic cells. The relative level of shootin1b activation (phospho-shootin1b/shootin1b)
213 was 120% higher on the CCL19 high side than on the low side (Figure 4G).

214 To examine a role of the polarized shootin1b phosphorylation (Figure 4F-G), we
215 expressed wild-type shootin1b (shootin1b-WT), unphosphorylated shootin1b mutant
216 (shootin1b-AA), in which Ser101 and Ser249 are replaced by alanine, and phosphomimic
217 shootin1b mutant (shootin1b-DD), in which these residues are replaced by aspartate, in
218 shootin1b KO dendritic cells. As expected, expression of shootin1b-WT, but not
219 shootin1b-AA, rescued the reductions in both migration speed and chemotaxis index of
220 shootin1b KO dendritic cells (Figure 4D-E, H-I). On the other hand, shootin1b-DD
221 rescued the reduction in migration speed (red n.s., Figure 4D, J) but not the reduction in
222 chemotaxis index (red asterisks, Figure 4E). Since shootin1b-DD is constitutively active
223 and cannot be regulated under the CCL19 signaling, we conclude that the polarized
224 shootin1b activation within dendritic cells drives the directional chemotaxis induced by
225 CCL19 gradients.
226

227 **Shootin1b-and L1-mediated dendritic cell migration is laminin-sensitive and**
228 **integrin-independent**
229 As shootin1b- and L1-mediated adhesion-clutch is enhanced by laminin (Figure 2E), we
230 next analyzed a role of laminins in chemotaxis. Removal of Matrigel, that contains
231 laminins, from the 3D environment decreased both the migration speed and chemotaxis
232 index of CCL19-induced dendritic cell chemotaxis (Figure 5A-C).
233 Talin couples F-actins with the cell adhesion molecules integrins as a clutch-
234 linker molecule[6,48]. However, shootin1b did not interact with β1- or β2-integrin (Figure
235 S6A) which are expressed in dendritic cells[40]. *Talin* has two isoforms, talin1 and talin2;
236 talin2 is not detected in dendritic cells[49]. Talin1 knockdown (Figure S6B) did not affect
237 the migration speed or chemotaxis index of WT and shootin1b KO dendritic cells under
238 CCL19 gradients (Video S9, Figure 5D-F), consistent with the previous report that
239 integrin ablation does not affect dendritic cell migration *in vitro* and *in vivo*[11]. These data
240 suggest that shootin1b and L1 mediate laminin-sensitive and integrin-independent
241 dendritic cell migration.
242
243 **Shootin1b drives dendritic cell migration in tissues**
244 Next, we examined whether shootin1b mediates the dendritic cell chemotaxis from the
245 skin to lymph nodes in response to CCL19 gradients[44-46]. WT dendritic cells labelled with
246 CMTPX and shootin1b KO dendritic cells labelled with CMFDA were mixed in a 1 : 1
247 ratio, and injected into the mouse footpad (Figure 5G). Twenty-four hours following the
248 injection, the popliteal lymph nodes were excised, and the number of WT and shootin1b
249 KO dendritic cells that had migrated into the lymph nodes was analyzed (Figure 5H). The
250 ratio of shootin1b KO dendritic cells that migrated into lymph nodes was significantly
251 lower than that of WT dendritic cells (Figure 5I), indicating that shootin1b KO inhibits
252 dendritic cell migration into the lymph nodes. To further examine the migration of
253 dendritic cells within the lymph nodes, CMFDA-labeled WT dendritic cells and CMTPX-
254 labeled shootin1b KO dendritic cells were mixed in a 1 : 1 ratio, and placed on the lymph
255 node slices. After 1h, dendritic cells migrated in the slices were observed by confocal
256 microscopy (Figure S7A, Video S10). Shootin1b KO led to a significant decrease in
257 migration speed of dendritic cells within the slices (Figure S7B). Collectively, these
258 results indicate that shootin1b drives dendritic cell migration in tissues.

259

260 **Aberrant activity of shootin1b promotes glioblastoma cell motility**

261 Finally, we investigated the motility of highly invasive glioblastoma cells. Although
262 shootin1b expression was undetectable in normal human and mouse brain-derived
263 astrocytes, immunoblot analysis detected a significant amount of shootin1b in
264 glioblastoma cells derived from a human patient (KNBTG-8) (Figure 6A). In addition,
265 L1 and cortactin, but do not shootin1a, was detected in these cells (Figure S8A). During
266 their invasion within the brain tissue, glioblastoma cells extend long protrusions called
267 tumor microtubes at the front[50,51]. We observed similar protrusions at the front of
268 glioblastoma cells in culture (Figure 6B). Shootin1b colocalized with F-actins at the tip
269 of the tumor microtubes (arrowheads, Figure 6B). Their migration speed in 3D Matrigel
270 was 0.16 ± 0.01 μm/min and 3.7 times faster than that of normal human astrocytes (Figure
271 6C-D, Video S11).

272 In control glioblastoma cells, F-actins moved retrogradely at 1.7 ± 0.3 μm/min
273 at the tip of the tumor microtubes (Figure 6E-F, Video S12), resulting in the generation of
274 a traction force of 26.4 ± 4.1 Pa there (Figure 6G, I, Video S13). Shootin1b knockdown
275 (Figure S8B) accelerated the F-actin flow (Figure 6F, Video S12) and led to 39%
276 reduction in the traction force (Figure 6H-I, Video S13), indicating that shootin1b
277 mediates a weak adhesion-clutch at the tip of the tumor microtubes. Furthermore,
278 shootin1b knockdown and shootin1-DN expression inhibited the migration speed of
279 glioblastoma cells by 43% and 40%, respectively (Figure 7A-F, Video S11).

280 To further analyze a possible role of shootin1b in glioblastoma invasion in tissue,
281 we prepared brain cortex organoids from human induced pluripotent stem (iPS) cells.
282 Equal numbers of the control cells, labeled with mCherry, and shootin1b-knockdown
283 cells (Figure S8C), labeled with EGFP, were combined; the resulting tumor spheroids
284 were co-cultured with the organoid for 72 h to facilitate fusion between them. They were
285 then cultured for further 5 days to allow the glioblastoma cells to invade into the organoids,
286 and their migration distance in the organoid was analyzed (Figure 7G-H). As shown in
287 Figure 7I, shootin1b knockdown significantly inhibited the glioblastoma invasion into the
288 brain cortex organoid. Thus, we conclude that the aberrant activity of the actin-substrate
289 coupling involving shootin1b promotes the glioblastoma cell motility.

290

291 **DISCUSSION**

292 **Weak adhesion-clutch for rapid cell migration**

293 The classical adhesion-clutch paradigm alone cannot explain accumulating experimental
294 data on cell migration. As examples, although disruption of the integrin-based adhesion-
295 clutch inhibits migration of melanoma cells and mast cells[52,53], it does not delay rapid
296 leukocyte migration[10,11,13] and paradoxically facilitates fibroblast motility[7]. In addition,
297 integrin activation inhibits T cell motility[10].

298 This study identified an integrin-independent adhesion-clutch machinery
299 involving shootin1b and L1 that drives rapid dendritic cell migration. Notably, shootin1b
300 and L1 slipped backwards against the adhesive substrate without forming stable
301 adhesions. This slippery actin-substrate coupling transmitted weak backward forces at
302 levels of 10 Pa. The integrin-based adhesion-clutch also undergoes similar retrograde
303 slippage during the initial stages of FA stabilization[5,54]. However, in mesenchymal cells,
304 it generates large traction force that reaches to kPa levels during tension-dependent
305 mechanosensing and FA maturation[8,9,55-58]. As transmission of large forces requires strong
306 adhesion, which impedes cell migration[14,18,59], the strong forces transmitted by mature
307 FAs would be rather suitable for immobilizing cells against mechanical stress. In fact,
308 fibroblasts do not undergo rapid migration under physiological conditions, and increasing
309 substrate stiffness decreases their random motility[60] while increasing traction force[9].

310 By integrating these previous and present data, we propose that the adhesion-
311 clutch can mediate both cell motility and immobilization depending on the force
312 amplitude; the weak adhesion-clutch is well-suited for rapid cell migration, without
313 forming strong adhesions (Figure 7J). In this regard, the integrin-mediated adhesion-
314 clutch can propel cell migration in a low adhesion context. We consider that the weak
315 adhesion-clutch is mechanistically consistent with the friction-based model[15-19], and may
316 cooperate with the adhesion-independent mechanisms[11,49,61,62] to propel efficient cell
317 migration.

318

319 **Driving cell migration in response to environmental chemicals**

320 Our data show that the present adhesion-dependent machinery enables cell migration
321 guided by the adhesive ligands in the environment. The ECM protein laminin on the
322 adhesive substrate enhanced the L1-substrate coupling (Figure 2D-E), thereby

323 accelerating dendritic cell migration in an haptokinetic manner (Figure 5A-C). Previous
324 studies have shown that neuronal shootin1a interacts not only with L1 but also with other
325 immunoglobulin-superfamily cell adhesion molecules, cadherin and DCC[29,63], raising the
326 possibility that the adhesion-clutch system involving shootin1b responds to multiple
327 adhesive ligands in the environment. Furthermore, shootin1b drives chemotaxis through
328 its polarized activation within cells under CCL19 signaling and Pak1-mediated shootin1b
329 phosphorylation (Figure 4F-J). Pak1 is regulated by Rac1 and Cdc42, which are shared
330 key signaling molecules activated by multiple chemoattractants[64-66]. The present
331 adhesion-clutch machinery could be tuned in response to a variety of environmental
332 chemicals, thereby regulating the speed and direction of cell migration and motility.
333
334 **Shootin1b promotes glioblastoma cell motility**
335 The present study extends the versatility of the shootin1b- and L1-mediated adhesion-
336 clutch by demonstrating that its aberrant activity enhances glioblastoma cell motility.
337 Glioblastoma is highly invasive, infiltrating and damaging surrounding brain tissue[24,67].
338 They are rapidly integrated into neural networks[25], and actively invade along white matter
339 tracts and blood vessels[68,69]. L1 on glioblastoma cells can directly interact with L1
340 expressed on neurons and oligodendrocytes that form neural networks[70] and with
341 laminins localized in the basement membrane of blood vessels[71].
342 In addition, glioblastoma cells express various neurotransmitter receptors
343 including glutamate receptors[25,72], and recent studies demonstrated that neuron-
344 glioblastoma interactions through neurotransmitters promotes glioblastoma invasion
345 under receptor activation and calcium signaling[51,73]. Interestingly, glutamate released
346 from the presynapse activates the shootin1a-mediated adhesion-clutch under calcium
347 signaling and shootin1a phosphorylation, thereby promoting the expansion of post-
348 synaptic dendritic spines[29]. Collectively, these data raise the possibility that the adhesion-
349 clutch involving shootin1b and L1 could potentially mediate haptotactic and neuron-
350 driven glioblastoma invasion in the brain.
351 Despite the availability of clinical treatments, including surgery, radiotherapy
352 and chemotherapy, glioblastoma patients have a poor clinical prognosis[74,75]. Consistent
353 with the previous report that shootin1b is undetectable in the adult mouse brain[30], we were
354 unable to detect it in normal human and mouse brain-derived astrocytes. Importantly,

355 shootin1b knockdown and shootin1-DN expression decreased the glioblastoma motility,
356 providing a potential target for specific inhibition of glioblastoma invasion in the adult
357 brain.
358 In conclusion, we present a weak adhesion-clutch suitable for driving
359 physiologically controlled and pathologically enhanced rapid cell migration.
360
361 **Limitations of the study**
362 The weak adhesion-clutch paradigm is limited in that it is based on the data obtained from
363 the shootin1b- and L1-mediated adhesion-clutch. Any adhesion-clutch mediated by other
364 molecules could propel cell migration in a low adhesion context. In this regard, shootin1b
365 depletion did not completely inhibit traction forces produced by dendritic cells and
366 glioblastoma cells which were paralleled by their partial inhibition of migration. Thus,
367 future investigation of other molecular machinery and other cell types, along with the
368 measurements of force and migration velocity, will be important for obtaining a more
369 generalized view of the weak adhesion-clutch in cell migration.
370 This work provides a potential target shootin1b for glioblastoma treatment.
371 However, it is important to note that the cell migration assays were performed in Matrigel
372 and human brain cortex organoids, where the normal neural networks are not established.
373 In addition, glioblastoma is heterogeneous[72] and we analyzed the effect of shootin1b
374 knockdown using cells derived from a single human patient. Future work to analyze
375 shootin1b-reduced glioblastoma invasion in brain tissue, using cells expressing different
376 levels of shootin1b from multiple patients, will contribute to a more complete
377 understanding of glioblastoma invasion and help guide future therapeutic strategies.

RESOURCE AVAILABILITY

Lead Contact

Further information and requests for resources and reagents should be directed to and will be fulfilled by the Lead Contact, Naoyuki Inagaki (ninagaki@bs.naist.jp).

Materials availability

All unique materials generated in this study are available from the Lead Contact without restriction.

Data and code availability

Source data of immunoblot and statistical analyses in the figures are available at Mendeley Data (https://data.mendeley.com/datasets/vvhs642dvz/1). Any additional information required to reanalyze the data reported in this paper are available from the lead contact upon request.

ACKNOWLEDGMENTS

We thank Dr. Peter Friedl (Radboud University Medical Centre), Dr. Michael Sixt (Institute of Science and Technology Austria), Dr. Ewa Paluch (University of Cambridge), Dr. Tim Lämmermann (Max Planck Inst of Immunobiology and Epigenetics) and Dr. Takunori Minegishi (Nara Institute of Science and Technology) for valuable discussions; Mieko Ueda and Kazumi Maekawa for technical support; and Satoko Shimamura for kind encouragement. This research was supported in part by AMED under Grant Number JP17gm0810011 (N.I.), JSPS KAKENHI (JP19H03223, N.I.) JSPS Grants-in-Aid for Early-Career Scientists (JP19K16127, K.B.), and the Osaka Medical Research Foundation for Incurable Diseases (K.B.).

AUTHOR CONTRIBUTIONS

K.B., D.K., T. K., Y. K., and N.I. designed the experiments. K.B., A. F.-K., M. M., R. T., Z. X, Y. N., M. S., Y. H., H. K.-K., A. K., Y. U., and Y. K. performed the experiments and data analysis. K.B, D.K., Y.K., and N.I wrote the manuscript. N.I. supervised the project. All authors discussed the results and commented on the manuscript.

410

411 **DECLARATION OF INTERESTS**

412 K.B., A.K.-F., A.K., D.K., Y.K., and N.I., have filed a patent application related to this
413 work.

414

415 **STAR METHODS**

416 Detailed methods are provided in the online version of this paper and include the
417 following:

418 - **KEY RESOURCE TABLE**
419 - **EXPERIMENTAL MODEL AND STUDY PARTICIPANT DETAILS**
420 - Ethical considerations
421 - Generation of shootin1 knockout mice
422 - Bone marrow-derived dendritic cell culture and induction of dendritic cell
423 maturation
424 - Transfection of dendritic cells
425 - Glioblastoma cell culture and transfection
426 - HEK293T cell and human astrocyte culture and transfection
427 - Mouse primary astrocyte cell culture
428 - Generation of brain cortex organoid derived from human iPS cells
429 - **METHOD DETAILS**
430 - DNA construction and RNAi experiment
431 - RNAi experiment mediated by lentivirus carrying short hairpin RNA
432 - Invasion assay using brain cortex organoid
433 - Flow cytometry analysis
434 - Immunocytochemistry
435 - Immunoprecipitation and Immunoblot
436 - Chemotaxis assay and random migration assay
437 - Glioblastoma cell and astrocyte 3D migration assay
438 - Fluorescent speckle imaging
439 - Traction force microscopy
440 - Analysis of the correlation between the directions of force and cell migration

441 ○ Analysis of dendritic cell migration in lymph node slice
442 ○ *In vivo* dendritic cell migration assay
443 ○ Generation of CCL19 gradients for immunocytochemistry
444 • **QUANTIFICATIONS AND STATISTICAL ANALYSIS**
445
446 **SUPPLEMENTAL INFORMATION**
447 Supplemental information can be found online at…….
448
449 **REFERENCES**

450 1. Wang, Y.L. (1985). Exchange of actin subunits at the leading edge of living fibroblasts:
451 possible role of treadmilling. J. Cell Biol. *101*, 597-602.
452 2. Theriot, J.A., and Mitchison, T.J. (1991). Actin microfilament dynamics in locomoting
453 cells. Nature *352*, 126-131.
454 3. Mitchison, T., and Kirschner, M. (1988). Cytoskeletal dynamics and nerve growth.
455 Neuron *1*, 761-772.
456 4. Case, L.B., and Waterman, C.M. (2015). Integration of actin dynamics and cell adhesion
457 by a three-dimensional, mechanosensitive molecular clutch. Nat. Cell Biol. *17*, 955-963.
458 5. Hu, K., Ji, L., Applegate, K.T., Danuser, G., and Waterman-Storer, C.M. (2007).
459 Differential transmission of actin motion within focal adhesions. Science *315*, 111-115.
460 6. Zhang, X., Jiang, G., Cai, Y., Monkley, S.J., Critchley, D.R., and Sheetz, M.P. (2008).
461 Talin depletion reveals independence of initial cell spreading from integrin activation and
462 traction. Nat. Cell Biol. *10*, 1062-1068.
463 7. Thievessen, I., Thompson, P.M., Berlemont, S., Plevock, K.M., Plotnikov, S.V., Zemljic-
464 Harpf, A., Ross, R.S., Davidson, M.W., Danuser, G., Campbell, S.L., and Waterman, C.M.
465 (2013). Vinculin-actin interaction couples actin retrograde flow to focal adhesions, but is
466 dispensable for focal adhesion growth. J. Cell Biol. *202*, 163-177.
467 8. Moore, S.W., Roca-Cusachs, P., and Sheetz, M.P. (2010). Stretchy proteins on stretchy
468 substrates: the important elements of integrin-mediated rigidity sensing. Dev Cell *19*,
469 194-206.
470 9. Elosegui-Artola, A., Oria, R., Chen, Y., Kosmalska, A., Perez-Gonzalez, C., Castro, N.,
471 Zhu, C., Trepat, X., and Roca-Cusachs, P. (2016). Mechanical regulation of a molecular
472 clutch defines force transmission and transduction in response to matrix rigidity. Nat. Cell
473 Biol. *18*, 540-548.
474 10. Friedl, P., Entschladen, F., Conrad, C., Niggemann, B., and Zanker, K.S. (1998). CD4+
475 T lymphocytes migrating in three-dimensional collagen lattices lack focal adhesions and

476 utilize beta1 integrin-independent strategies for polarization, interaction with collagen
477 fibers and locomotion. Eur. J. Immunol. *28*, 2331-2343.
478 11. Lammermann, T., Bader, B.L., Monkley, S.J., Worbs, T., Wedlich-Soldner, R., Hirsch, K.,
479 Keller, M., Forster, R., Critchley, D.R., Fassler, R., and Sixt, M. (2008). Rapid leukocyte
480 migration by integrin-independent flowing and squeezing. Nature *453*, 51-55.
481 12. Paluch, E.K., Aspalter, I.M., and Sixt, M. (2016). Focal Adhesion-Independent Cell
482 Migration. Annu. Rev. Cell Dev. Biol. *32*, 469-490.
483 13. Paterson, N., and Lammermann, T. (2022). Macrophage network dynamics depend on
484 haptokinesis for optimal local surveillance. Elife *11*, e75354.
485 14. Schmidt, S., and Friedl, P. (2010). Interstitial cell migration: integrin-dependent and
486 alternative adhesion mechanisms. Cell Tissue Res. *339*, 83-92.
487 15. Bergert, M., Erzberger, A., Desai, R.A., Aspalter, I.M., Oates, A.C., Charras, G., Salbreux,
488 G., and Paluch, E.K. (2015). Force transmission during adhesion-independent migration.
489 Nat. Cell Biol. *17*, 524-529.
490 16. Hons, M., Kopf, A., Hauschild, R., Leithner, A., Gaertner, F., Abe, J., Renkawitz, J., Stein,
491 J.V., and Sixt, M. (2018). Chemokines and integrins independently tune actin flow and
492 substrate friction during intranodal migration of T cells. Nat. Immunol. *19*, 606-616.
493 17. Ruprecht, V., Wieser, S., Callan-Jones, A., Smutny, M., Morita, H., Sako, K., Barone, V.,
494 Ritsch-Marte, M., Sixt, M., Voituriez, R., and Heisenberg, C.P. (2015). Cortical
495 contractility triggers a stochastic switch to fast amoeboid cell motility. Cell *160*, 673-685.
496 18. Liu, Y.J., Le Berre, M., Lautenschlaeger, F., Maiuri, P., Callan-Jones, A., Heuze, M.,
497 Takaki, T., Voituriez, R., and Piel, M. (2015). Confinement and low adhesion induce fast
498 amoeboid migration of slow mesenchymal cells. Cell *160*, 659-672.
499 19. Hawkins, R.J., Poincloux, R., Benichou, O., Piel, M., Chavrier, P., and Voituriez, R.
500 (2011). Spontaneous contractility-mediated cortical flow generates cell migration in
501 three-dimensional environments. Biophys. J. *101*, 1041-1045.
502 20. Aoun, L., Farutin, A., Garcia-Seyda, N., Negre, P., Rizvi, M.S., Tlili, S., Song, S., Luo, X.,
503 Biarnes-Pelicot, M., Galland, R., et al. (2020). Amoeboid swimming is propelled by
504 molecular paddling in lymphocytes. Biophys. J. *119*, 1157-1177.
505 21. Yamada, K.M., and Sixt, M. (2019). Mechanisms of 3D cell migration. Nat. Rev. Mol. Cell
506 Biol. *20*, 738-752.
507 22. Lammermann, T., and Sixt, M. (2009). Mechanical modes of 'amoeboid' cell migration.
508 Curr. Opin. Cell Biol. *21*, 636-644.
509 23. Friedl, P. (2004). Prespecification and plasticity: shifting mechanisms of cell migration.
510 Curr. Opin. Cell Biol. *16*, 14-23.
511 24. Cuddapah, V.A., Robel, S., Watkins, S., and Sontheimer, H. (2014). A neurocentric

512 perspective on glioma invasion. Nat. Rev. Neurosci. *15*, 455-465.
513 25. Tetzlaff, S.K., Reyhan, E., Layer, N., Bengtson, C.P., Heuer, A., Schroers, J., Faymonville,
514 A.J., Langeroudi, A.P., Drewa, N., Keifert, E., et al. (2025). Characterizing and targeting
515 glioblastoma neuron-tumor networks with retrograde tracing. Cell *188*, 1–22.
516 26. Toriyama, M., Shimada, T., Kim, K.B., Mitsuba, M., Nomura, E., Katsuta, K., Sakumura,
517 Y., Roepstorff, P., and Inagaki, N. (2006). Shootin1: A protein involved in the
518 organization of an asymmetric signal for neuronal polarization. J. Cell Biol. *175*, 147-157.
519 27. Shimada, T., Toriyama, M., Uemura, K., Kamiguchi, H., Sugiura, T., Watanabe, N., and
520 Inagaki, N. (2008). Shootin1 interacts with actin retrograde flow and L1-CAM to promote
521 axon outgrowth. J. Cell Biol. *181*, 817-829.
522 28. Kubo, Y., Baba, K., Toriyama, M., Minegishi, T., Sugiura, T., Kozawa, S., Ikeda, K., and
523 Inagaki, N. (2015). Shootin1-cortactin interaction mediates signal-force transduction for
524 axon outgrowth. J. Cell Biol. *210*, 663-676.
525 29. Kastian, R.F., Minegishi, T., Baba, K., Saneyoshi, T., Katsuno-Kambe, H., Saranpal, S.,
526 Hayashi, Y., and Inagaki, N. (2021). Shootin1a-mediated actin-adhesion coupling
527 generates force to trigger structural plasticity of dendritic spines. Cell Rep. *35*, 109130.
528 30. Higashiguchi, Y., Katsuta, K., Minegishi, T., Yonemura, S., Urasaki, A., and Inagaki, N.
529 (2016). Identification of a shootin1 isoform expressed in peripheral tissues. Cell Tissue
530 Res. *366*, 75-87.
531 31. Minegishi, T., Kastian, R., and Inagaki, N. (2021). Single speckle imaging using a standard
532 epi-fluorescent microscope and traction force microscopy at nerve growth cones. J. Vis.
533 Exp., e63227.
534 32. Maddaluno, L., Verbrugge, S.E., Martinoli, C., Matteoli, G., Chiavelli, A., Zeng, Y.,
535 Williams, E.D., Rescigno, M., and Cavallaro, U. (2009). The adhesion molecule L1
536 regulates transendothelial migration and trafficking of dendritic cells. J. Exp. Med. *206*,
537 623-635.
538 33. Hall, H., Carbonetto, S., and Schachner, M. (1997). L1/HNK-1 carbohydrate- and beta 1
539 integrin-dependent neural cell adhesion to laminin-1. J. Neurochem. *68*, 544-553.
540 34. Colombo, F., and Meldolesi, J. (2015). L1-CAM and N-CAM: From adhesion proteins to
541 pharmacological targets. Trends Pharmacol. Sci. *36*, 769-781.
542 35. Sixt, M., Kanazawa, N., Selg, M., Samson, T., Roos, G., Reinhardt, D.P., Pabst, R., Lutz,
543 M.B., and Sorokin, L. (2005). The conduit system transports soluble antigens from the
544 afferent lymph to resident dendritic cells in the T cell area of the lymph node. Immunity
545 *22*, 19-29.
546 36. Drumea-Mirancea, M., Wessels, J.T., Muller, C.A., Essl, M., Eble, J.A., Tolosa, E., Koch,
547 M., Reinhardt, D.P., Sixt, M., Sorokin, L., et al. (2006). Characterization of a conduit

548 system containing laminin-5 in the human thymus: a potential transport system for small
549 molecules. J. Cell Sci. *119*, 1396-1405.
550 37. Lammermann, T., Renkawitz, J., Wu, X., Hirsch, K., Brakebusch, C., and Sixt, M. (2009).
551 Cdc42-dependent leading edge coordination is essential for interstitial dendritic cell
552 migration. Blood *113*, 5703-5710.
553 38. Ricart, B.G., Yang, M.T., Hunter, C.A., Chen, C.S., and Hammer, D.A. (2011). Measuring
554 traction forces of motile dendritic cells on micropost arrays. Biophys. J. *101*, 2620-2628.
555 39. Baba, K., Yoshida, W., Toriyama, M., Shimada, T., Manning, C.F., Saito, M., Kohno, K.,
556 Trimmer, J.S., Watanabe, R., and Inagaki, N. (2018). Gradient-reading and mechano-
557 effector machinery for netrin-1-induced axon guidance. Elife *7*, e34593.
558 40. Renkawitz, J., Schumann, K., Weber, M., Lammermann, T., Pflicke, H., Piel, M., Polleux,
559 J., Spatz, J.P., and Sixt, M. (2009). Adaptive force transmission in amoeboid cell migration.
560 Nat. Cell Biol. *11*, 1438-1443.
561 41. Sanchez-Sanchez, N., Riol-Blanco, L., and Rodriguez-Fernandez, J.L. (2006). The
562 multiple personalities of the chemokine receptor CCR7 in dendritic cells. J. Immunol. *176*,
563 5153-5159.
564 42. Lu, M., Xu, C., Zhang, Q., Wu, X., Tang, L., Wang, X., Wu, J., and Wu, X. (2018).
565 Inhibition of p21-activated kinase 1 attenuates the cardinal features of asthma through
566 suppressing the lymph node homing of dendritic cells. Biochem. Pharmacol. *154*, 464-473.
567 43. Toriyama, M., Kozawa, S., Sakumura, Y., and Inagaki, N. (2013). Conversion of a signal
568 into forces for axon outgrowth through Pak1-mediated shootin1 phosphorylation. Curr.
569 Biol. *23*, 529-534.
570 44. Alvarez, D., Vollmann, E.H., and von Andrian, U.H. (2008). Mechanisms and
571 consequences of dendritic cell migration. Immunity *29*, 325-342.
572 45. Pfeiffer, F., Kumar, V., Butz, S., Vestweber, D., Imhof, B.A., Stein, J.V., and Engelhardt,
573 B. (2008). Distinct molecular composition of blood and lymphatic vascular endothelial cell
574 junctions establishes specific functional barriers within the peripheral lymph node. Eur. J.
575 Immunol. *38*, 2142-2155.
576 46. Sobocinski, G.P., Toy, K., Bobrowski, W.F., Shaw, S., Anderson, A.O., and Kaldjian, E.P.
577 (2010). Ultrastructural localization of extracellular matrix proteins of the lymph node
578 cortex: evidence supporting the reticular network as a pathway for lymphocyte migration.
579 BMC Immunol. *11*, 42.
580 47. Haessler, U., Pisano, M., Wu, M., and Swartz, M.A. (2011). Dendritic cell chemotaxis in
581 3D under defined chemokine gradients reveals differential response to ligands CCL21 and
582 CCL19. Proc. Natl. Acad. Sci. U. S. A. *108*, 5614-5619.
583 48. Giannone, G., Mege, R.M., and Thoumine, O. (2009). Multi-level molecular clutches in

584 motile cell processes. Trends Cell Biol. *19*, 475-486.
585 49. Reversat, A., Gaertner, F., Merrin, J., Stopp, J., Tasciyan, S., Aguilera, J., de Vries, I.,
586 Hauschild, R., Hons, M., Piel, M., et al. (2020). Cellular locomotion using environmental
587 topography. Nature *582*, 582-585.
588 50. Osswald, M., Jung, E., Sahm, F., Solecki, G., Venkataramani, V., Blaes, J., Weil, S.,
589 Horstmann, H., Wiestler, B., Syed, M., et al. (2015). Brain tumour cells interconnect to a
590 functional and resistant network. Nature *528*, 93-98.
591 51. Venkataramani, V., Yang, Y., Schubert, M.C., Reyhan, E., Tetzlaff, S.K., Wissmann, N.,
592 Botz, M., Soyka, S.J., Beretta, C.A., Pramatarov, R.L., et al. (2022). Glioblastoma hijacks
593 neuronal mechanisms for brain invasion. Cell *185*, 2899-2917 e2831.
594 52. Maaser, K., Wolf, K., Klein, C.E., Niggemann, B., Zanker, K.S., Brocker, E.B., and Friedl,
595 P. (1999). Functional hierarchy of simultaneously expressed adhesion receptors: integrin
596 alpha2beta1 but not CD44 mediates MV3 melanoma cell migration and matrix
597 reorganization within three-dimensional hyaluronan-containing collagen matrices. Mol.
598 Biol. Cell *10*, 3067-3079.
599 53. Kaltenbach, L., Martzloff, P., Bambach, S.K., Aizarani, N., Mihlan, M., Gavrilov, A.,
600 Glaser, K.M., Stecher, M., Thunauer, R., Thiriot, A., et al. (2023). Slow integrin-
601 dependent migration organizes networks of tissue-resident mast cells. Nat. Immunol. *24*,
602 915-924.
603 54. Aratyn-Schaus, Y., and Gardel, M.L. (2010). Transient frictional slip between integrin
604 and the ECM in focal adhesions under myosin II tension. Curr. Biol. *20*, 1145-1153.
605 55. del Rio, A., Perez-Jimenez, R., Liu, R., Roca-Cusachs, P., Fernandez, J.M., and Sheetz,
606 M.P. (2009). Stretching single talin rod molecules activates vinculin binding. Science *323*,
607 638-641.
608 56. Changede, R., Xu, X., Margadant, F., and Sheetz, M.P. (2015). Nascent integrin adhesions
609 form on all matrix rigidities after integrin activation. Dev. Cell *35*, 614-621.
610 57. Sun, Z., Guo, S.S., and Fassler, R. (2016). Integrin-mediated mechanotransduction. J. Cell
611 Biol. *215*, 445-456.
612 58. Elosegui-Artola, A., Trepat, X., and Roca-Cusachs, P. (2018). Control of
613 mechanotransduction by molecular clutch dynamics. Trends Cell Biol. *28*, 356-367.
614 59. Palecek, S.P., Loftus, J.C., Ginsberg, M.H., Lauffenburger, D.A., and Horwitz, A.F.
615 (1997). Integrin-ligand binding properties govern cell migration speed through cell-
616 substratum adhesiveness. Nature *385*, 537-540.
617 60. Kuboki, T., Ebata, H., Matsuda, T., Arai, Y., Nagai, T., and Kidoaki, S. (2020).
618 Hierarchical development of motile polarity in durotactic cells just crossing an elasticity
619 boundary. Cell Struct. Funct. *45*, 33-43.

620 61. Petrie, R.J., Koo, H., and Yamada, K.M. (2014). Generation of compartmentalized
621 pressure by a nuclear piston governs cell motility in a 3D matrix. Science *345*, 1062-1065.
622 62. Stroka, K.M., Jiang, H., Chen, S.H., Tong, Z., Wirtz, D., Sun, S.X., and Konstantopoulos,
623 K. (2014). Water permeation drives tumor cell migration in confined microenvironments.
624 Cell *157*, 611-623.
625 63. Qiu, Z., Minegishi, T., Aoki, D., Abe, K., Baba, K., and Inagaki, N. (2024). Adhesion-
626 clutch between DCC and netrin-1 mediates netrin-1-induced axonal haptotaxis. Front.
627 Mol. Neurosci. *17*, 1307755.
628 64. Wu, D. (2005). Signaling mechanisms for regulation of chemotaxis. Cell Res. *15*, 52-56.
629 65. Lawson, C.D., and Ridley, A.J. (2018). Rho GTPase signaling complexes in cell migration
630 and invasion. J. Cell Biol. *217*, 447-457.
631 66. Weiss, F., Lauffenburger, D., and Friedl, P. (2022). Towards targeting of shared
632 mechanisms of cancer metastasis and therapy resistance. Nat. Rev. Cancer *22*, 157-173.
633 67. Demuth, T., and Berens, M.E. (2004). Molecular mechanisms of glioma cell migration
634 and invasion. J. Neurooncol. *70*, 217-228.
635 68. Watkins, S., Robel, S., Kimbrough, I.F., Robert, S.M., Ellis-Davies, G., and Sontheimer,
636 H. (2014). Disruption of astrocyte-vascular coupling and the blood-brain barrier by
637 invading glioma cells. Nat, Commun, *5*, 4196.
638 69. Drumm, M.R., Dixit, K.S., Grimm, S., Kumthekar, P., Lukas, R.V., Raizer, J.J., Stupp, R.,
639 Chheda, M.G., Kam, K.L., McCord, M., et al. (2020). Extensive brainstem infiltration, not
640 mass effect, is a common feature of end-stage cerebral glioblastomas. Neuro. Oncol. *22*,
641 470-479.
642 70. Fields, R.D. (2015). A new mechanism of nervous system plasticity: activity-dependent
643 myelination. Nat. Rev. Neurosci. *16*, 756-767.
644 71. Lau, L.W., Cua, R., Keough, M.B., Haylock-Jacobs, S., and Yong, V.W. (2013).
645 Pathophysiology of the brain extracellular matrix: a new target for remyelination. Nat. Rev.
646 Neurosci. *14*, 722-729.
647 72. Neftel, C., Laffy, J., Filbin, M.G., Hara, T., Shore, M.E., Rahme, G.J., Richman, A.R.,
648 Silverbush, D., Shaw, M.L., Hebert, C.M., et al. (2019). An integrative model of cellular
649 states, plasticity, and genetics for glioblastoma. Cell *178*, 835-849 e821.
650 73. Winkler, F., Venkatesh, H.S., Amit, M., Batchelor, T., Demir, I.E., Deneen, B., Gutmann,
651 D.H., Hervey-Jumper, S., Kuner, T., Mabbott, D., et al. (2023). Cancer neuroscience::
652 state of the field, emerging directions. Cell *186*, 1689-1707.
653 74. Ostrom, Q.T., Bauchet, L., Davis, F.G., Deltour, I., Fisher, J.L., Langer, C.E., Pekmezci,
654 M., Schwartzbaum, J.A., Turner, M.C., Walsh, K.M., et al. (2014). The epidemiology of
655 glioma in adults: a "state of the science" review. Neuro. Oncol. *16*, 896-913.

656 75. Weller, M., Wick, W., Aldape, K., Brada, M., Berger, M., Pfister, S.M., Nishikawa, R.,
657 Rosenthal, M., Wen, P.Y., Stupp, R., and Reifenberger, G. (2015). Glioma. Nat. Rev. Dis.
658 Primers *1*, 15017.
659 76. Lutz, M.B., Kukutsch, N., Ogilvie, A.L., Rossner, S., Koch, F., Romani, N., and Schuler,
660 G. (1999). An advanced culture method for generating large quantities of highly pure
661 dendritic cells from mouse bone marrow. J. Immunol. Methods *223*, 77-92.
662 77. Wang, W., Li, J., Wu, K., Azhati, B., and Rexiati, M. (2016). Culture and Identification of
663 Mouse Bone Marrow-Derived Dendritic Cells and Their Capability to Induce T
664 Lymphocyte Proliferation. Med. Sci. Monit. *22*, 244-250.
665 78. Bamba, Y., Shofuda, T., Kanematsu, D., Nonaka, M., Yamasaki, M., Okano, H., and
666 Kanemura, Y. (2014). Differentiation, polarization, and migration of human induced
667 pluripotent stem cell-derived neural progenitor cells co-cultured with a human glial cell
668 line with radial glial-like characteristics. Biochem. Biophys. Res. Commun. *447*, 683-688.
669 79. Eino, D., Tsukada, Y., Naito, H., Kanemura, Y., Iba, T., Wakabayashi, T., Muramatsu, F.,
670 Kidoya, H., Arita, H., Kagawa, N., et al. (2018). LPA4-Mediated Vascular Network
671 Formation Increases the Efficacy of Anti-PD-1 Therapy against Brain Tumors. Cancer
672 Res. *78*, 6607-6620.
673 80. Kim, H., Sa, J.K., Kim, J., Cho, H.J., Oh, H.J., Choi, D.H., Kang, S.H., Jeong, D.E., Nam,
674 D.H., Lee, H., et al. (2022). Recapitulated crosstalk between cerebral metastatic lung
675 cancer cells and brain perivascular tumor microenvironment in a microfluidic co-culture
676 chip. Adv Sci (Weinh) *9*, e2201785.
677 81. Inagaki, N., Fukui, H., Taguchi, Y., Wang, N.P., Yamatodani, A., and Wada, H. (1989).
678 Characterization of histamine H1-receptors on astrocytes in primary culture:
679 [3H]mepyramine binding studies. Eur. J. Pharmacol. *173*, 43-51.
680 82. Io, S., Iemura, Y., and Takashima, Y. (2021). Optimized protocol for naive human
681 pluripotent stem cell-derived trophoblast induction. STAR Protoc. *2*, 100921.
682 83. Watanabe, M., Buth, J.E., Vishlaghi, N., de la Torre-Ubieta, L., Taxidis, J., Khakh, B.S.,
683 Coppola, G., Pearson, C.A., Yamauchi, K., Gong, D., et al. (2017). Self-organized cerebral
684 organoids with human-specific features predict effective drugs to combat Zika virus
685 infection. Cell Rep. *21*, 517-532.
686 84. Lancaster, M.A., and Knoblich, J.A. (2014). Generation of cerebral organoids from human
687 pluripotent stem cells. Nat. Protoc. *9*, 2329-2340.
688 85. Minegishi, T., Uesugi, Y., Kaneko, N., Yoshida, W., Sawamoto, K., and Inagaki, N. (2018).
689 Shootin1b mediates a mechanical clutch to produce force for neuronal migration. Cell Rep.
690 *25*, 624-639.e626.
691 86. Azizi, L., Cowell, A.R., Mykuliak, V.V., Goult, B.T., Turkki, P., and Hytonen, V.P. (2021).

692 Cancer associated talin point mutations disorganise cell adhesion and migration. Sci. Rep.
693 *11*, 347.
694 87. Abe, K., Katsuno, H., Toriyama, M., Baba, K., Mori, T., Hakoshima, T., Kanemura, Y.,
695 Watanabe, R., and Inagaki, N. (2018). Grip and slip of L1-CAM on adhesive substrates
696 direct growth cone haptotaxis. Proc. Natl. Acad. Sci. U. S. A. *115*, 2764-2769.
697 88. Salmon, H., Rivas-Caicedo, A., Asperti-Boursin, F., Lebugle, C., Bourdoncle, P., and
698 Donnadieu, E. (2011). Ex vivo imaging of T cells in murine lymph node slices with
699 widefield and confocal microscopes. J. Vis. Exp., e3054.
700 89. Katakai, T., Habiro, K., and Kinashi, T. (2013). Dendritic cells regulate high-speed
701 interstitial T cell migration in the lymph node via LFA-1/ICAM-1. J. Immunol. *191*, 1188-
702 1199.
703 90. Kastian, R.F., Baba, K., Kaewkascholkul, N., Sasaki, H., Watanabe, R., Toriyama, M., and
704 Inagaki, N. (2023). Dephosphorylation of neural wiring protein shootin1 by PP1
705 phosphatase regulates netrin-1-induced axon guidance. J. Biol. Chem. *299*, 104687.
706

707 **STAR METHODS**

708 **KEY RESOURCES TABLE**

REAGENT or RESOURCE	SOURCE	IDENTIFIER
Antibodies		
Rabbit polyclonal anti-shootin1b	(Higashiguchi et al., 2016)	N/A
Rabbit polyclonal anti-shootin1a	(Baba et al., 2018)	N/A
Rabbit polyclonal anti-shootin1	(Toriyama et al., 2006)	N/A
Rabbit polyclonal anti-pSer101-shootin1	(Toriyama et al., 2013)	N/A
Rabbit polyclonal anti-pSer249-shootin1	(Toriyama et al., 2013)	N/A
Rabbit monoclonal anti-CCR7	Abcam	Cat# ab32527; RRID: AB_726208
Rabbit polyclonal anti-flag	MBL	Cat# PM020; RRID: AB_591224
Rabbit polyclonal anti-GFP	MBL	Cat# 598; RRID: AB_591816
Mouse monoclonal anti-L1 (C-2)	Santa Cruz	Cat# sc-514360; no RRID available
Mouse monoclonal anti-cortactin clone 4F11	Millipore	Cat# 05-180; RRID: AB_309647
Mouse monoclonal anti-actin clone C4	Millipore	Cat# MAB1501; RRID: AB_2223041
Mouse monoclonal anti-GFP	MBL	Cat# M048-3; RRID: AB_591823
Mouse monoclonal anti-myc	MBL	Cat# 562-5; RRID: AB_591116
Mouse monoclonal anti-flag	Sigma	Cat# F3165; RRID: AB_259529
Armenian hamster monoclonal anti-CD11c	BD Biosciences	Cat# 550283; RRID: AB_393578

Alexa Fluor 488 conjugated goat anti-rabbit	Thermo Fisher	Cat# A11008; RRID: AB143165
TRITC conjugated goat anti-rabbit	Thermo Fisher	Cat# A16101; RRID: AB_2534775
Alexa Fluor 594 conjugated goat anti-mouse	Invitrogen	Cat# A11032; RRID: AB_2534091
Alexa Fluor 488 conjugated goat anti-mouse	Invitrogen	Cat# A11029; RRID: AB_2534088
Alexa Fluor 594 conjugated goat anti-Armenian hamster	Jackson ImmunoResearch	Cat# 127-585-160; RRID: AB_2338999
Rat monoclonal anti-CD16/CD32 for Fc Block	BD Biosciences	Cat# 553142; RRID: AB_394657
Human monoclonal anti-IgG REA-FITC antibody	Miltenyi	Cat# 130-113-449; RRID: AB_2733688
Human monoclonal anti-mouse CD11c-FITC	Miltenyi	Cat# 130-110-837; RRID: AB_2654705
Human monoclonal anti-mouse-MHCII-FITC	Miltenyi	Cat# 130-112-386; RRID: AB_2652902
Human monoclonal anti-mouse-CD80-FITC	Miltenyi	Cat# 130-116-459; RRID: AB_2727556
HRP conjugated donkey anti-rabbit	GE Healthcare	Cat# NA934; RRID: AB_772206
HRP conjugated goat anti-mouse	Millipore	Cat# AP308P; RRID: AB_92635
Chemicals, peptides, and recombinant proteins		
Alexa Fluor 555 conjugated phalloidin	Cell Signaling	Cat# 8953
DAPI	Thermo Fisher	Cat# D1306
Recombinant mouse GM-CSF	Fujifilm	Cat# 077-04674
LPS	Sigma	Cat# L2880
EGF (for glioblastoma cell culture)	PeproTech	Cat# AF-100-15
FGF (for glioblastoma cell culture)	PeproTech	Cat# AF-100-18B
Leukemia inhibitory factor (for glioblastoma cell culture)	Millipore	Cat# LIF-1010

B27 supplement (for glioblastoma cell culture)	Thermo Fisher	Cat# 17504044
Heparin	Sigma	Cat# H3149
FGF (for generation of brain cortex organoid)	Sigma	Cat# F0291
ROCK inhibitor (Y-27632)	FUJIFILM	Cat# 036-24023
Wnt antagonists	Sigma	Cat# 681669
TGF-b inhibitor (SB-431542)	Tocris	Cat# 1614
B27 supplement without vitamin A (for generation of brain cortex organoid)	Gibco	Cat# 12587010
Matrigel (for generation of brain cortex organoid)	Corning	Cat# 354230
Leukemia inhibitory factor (for generation of brain cortex organoid)	Sigma	Cat# ESG1107
ProLong Gold	Thermo Fisher	Cat# P36930
CCL19	R&D Systems	Cat# 440-M3-025
PhosStop	Roche	Cat# 4906845001
Protein G-sepharose 4	GE Healthcare	Cat# 17061801
NVS- Pak1-1 (Pak1 inhibitor)	Sigma	Cat# SML1867-5MG
Hoechst (NucBlue)	Thermo Fisher	Cat# R37605
Collagen type I	KOKEN	Cat# IAC-50
Matrigel (for dendritic cell or glioblastoma cell 3D migration)	Corning	Cat# 356231
TMR ligand	Promega	Cat# G299A
Poly-D-lysine	Sigma	Cat# P6407-5MG
Laminin solution from mouse EHS tumor	FUJIFILM	Cat# 120-05751
Fluorescent nano beads (200 nm diameter)	Thermo Fisher	Cat# F8810
CMFDA	Invitrogen	Cat# C2925
CMTPX	Invitrogen	Cat# C34552
Low gelling-temperature agarose	Sigma	Cat# A0701
Polydimethylsiloxane (PDMS, Silpot 184)	Dow corning Toray	Cat# 3255981

Silicon oil (Barrier coat)	ShinEtsu	Cat# No. 6
Fetal Bovine Serum	Gibco	Cat# 10270106
Critical commercial assays		
Protein G-sepharose 4	GE Healthcare	Cat# 17061801
NEON electroporation system	Invitrogen	Cat# MPK5000
Buffer R (for NEON electroporation)	Invitrogen	Cat# MPK1025R
Nucleofector2B electroporation system	Lonza	Cat# AAB-1001
Neural stem cell nucleofector kit (for Nucleofector2B electroporation)	Lonza	Cat# VPG1004
Polyethylenimine MAX (PEI MAX)	Polysciences	Cat# 24765
Block-iT Pol II miR RNAi expression vector with GFP kit	Invitrogen	Cat# K493600
FuGENE HD Transfection Reagent	Promega	Cat# 31985062
μ-slide chemotaxis chamber	Ibidi	Cat# ib80326
Experimental models: cell lines		
HEK293T cell	ATCC	Cat# CRL_3216; RRID: CVCL_0063
Human brain astrocyte	Applied cell biology	Cat# ACBRI-371
iPSC B7 line (201B7 cell line)	RIKEN BioResource Research Center	RRID: CVCL_A324
Experimental models: Organisms/strains		
Mouse C57BL/6	Japan SLC; CLEA Japan	N/A
Mouse shootin1 KO	(Baba et al., 2018)	N/A
Oligonucleotides		
Genotyping primers	See Table S2	N/A
Shootin1b S101A, S101D, S249D, S249A primers	See Table S2	N/A
Integrin β1 or β2 intracellular domain primers	See Table S2	N/A
Lifeact top and bottom	See Table S2	N/A
Human shootin1b RNAi #1~#8	See Table S2	N/A
Mouse talin1 RNAi #1~#5	See Table S2	N/A
Recombinant DNA		

pFN21A-HaloTag-actin	(Minegishi et al., 2018)	N/A
pFN21A-Halotag-shootin1b	(Minegishi et al., 2018)	N/A
pFC14K-L1-HaloTag	(Abe et al., 2018)	N/A
pCAGGS-EGFP	(Baba et al., 2018)	N/A
pCAGGS-EGFP-shootin1 (1-125) (shootin1-DN)	(Baba et al., 2018)	N/A
Mouse talin1 full length WT-EGFP	Addgene	Cat# 166112 RRID: Addgene_166112
pCMV-flag	(Minegishi et al., 2018)	N/A
pCMV-flag-shootin1b WT	(Minegishi et al., 2018)	N/A
pCMV-flag-phospho mimic shootin1b (shootin1b DD)	This study	N/A
pCMV-flag-nonphospho mimic shootin1b (shootin1b AA)	This study	N/A
pAcGFP-C1	Clontech	Cat# 632470
pAcGFP- integrin β1 or β2 intracellular domain (ICD)	This study	N/A
L1 cDNA	(Baba et al., 2018)	N/A
pAcGFP-L1 intracellular domain (ICD)	This study	N/A
Control RNAi vector	This study	N/A
Human shootin1b RNAi vector (#1 ~ #8)	This study	N/A
Mouse talin1 RNAi vector (#1 ~ #5)	This study	N/A
pEGFP-N1	Clontech	Cat# 6085-1
Lifeact-EGFP	This study	N/A
Software and algorithms		
Fiji	National Institutes of Health	http://fiji.sc; RRID: SCR_002285
Microsoft Excel	Microsoft	https://www.microsoft.com/

GraphPad Prism7	GraphPad Software	https://www.graphpad.com/; RRID: SCR_002798
ZEN software	Carl Zeiss	https://www.zeiss.com/microscopy/int/products/microscope-software/zen.html; RRID: SCR_013672
Metamorph	Molecular Devices	N/A
LAS X	Leica	N/A
Cell Sorter Software	Sony	N/A

EXPERIMENTAL MODEL AND STUDY PARTICIPANT DETAILS

Ethical considerations

This study was carried out in accordance with the principle of the Helsinki Declaration. The use of glioblastoma tissues was approved by the Institutional Review Boards of Nara Institute of Science and Technology (approved number: No. 2018G32), Osaka National Hospital (approved number: No.713) and all collaborating institutions. Surgically removed brain tumor tissues were collected at Osaka National Hospital after obtaining written informed consent. iPSC experiments were conducted with prior approval from NCNP ethical Committee.

Generation of shootin1 KO mice

All relevant aspects of the experimental procedures were approved by the Institutional Animal Care and Use Committee of Nara Institute of Science and Technology. The generation of shootin1 KO mice is described elsewhere[39]. Chimeric mice were crossed with C57BL/6 mice for at least seven generations before analysis. Male and female shootin1 heterozygous mice were mated to obtain shootin1 KO mice; the offspring genotypes were checked by PCR with the following primers: Genotyping Fw1 (5'-CAGACTGCTACCCACTACCCCCTAC-3'), Genotyping Rv1 (5'-CCTAGAGCTGGACAGCGGATCTGAG-3'), Genotyping Fw2 (5'-CCCAGAAAGCGAAGGAACAAAGCTG-3'), and Genotyping Rv2 (5'-

731 ACCTTGCTCCTTCAAGCTGGTGATG-3')[29]. Six-to-eight-week-old mice were used
732 for dendritic cell culture[76,77].
733
734 **Bone marrow-derived dendritic cell culture and induction of dendritic cell**
735 **maturation**
736 Bone marrow-derived dendritic cells were prepared as described[73,74] with modifications.
737 Tibias and femurs were removed from the surrounding muscle tissue by sterile dissection
738 scissors, and then immersed in 70% ethanol for 5 min. Bones were washed with RPMI-
739 1640 medium (Fujifilm, catalog number: 189-02145) under sterile conditions. Both ends
740 of the bone were cut off with scissors. RPMI-1640 medium was sucked up using the 25-
741 gauge needle (TERUMO, catalog number: NN-2525R) equipped with 1 mL syringe
742 (TERUMO, catalog number: SS-01T). The needle was inserted into the bone cavity to
743 rinse the bone marrow out of the cavity into a sterile culture dish containing RPMI-1640
744 medium. The suspension of bone marrow-derived cells was filtered by 70 μm strainer
745 (Falcon, catalog number: 352350) and centrifuged at 190 G for 5 min. The supernatant
746 was discarded, and the cell pellet was resuspended in red blood cell lysis buffer (17 mM
747 Tris, 160 mM NH_4Cl, pH 7.2) for 8 min. Following the centrifugation, the supernatant
748 was discarded and the pellet was washed by PBS. The cell suspension in PBS was
749 centrifuged at 190 G for 5 min. The supernatant was discarded, and the pellet of bone
750 marrow-derived cells was resuspended in the complete RPMI-1640 medium
751 supplemented with 10 % fetal bovine serum (FBS, heat-inactivated, filtered) (Gibco:
752 catalog number: 10270-106), 100 U/mL Penicillin-100 μg/mL streptomycin (Nacalai,
753 catalog number: 26253-84), 2 mM GlutaMAX (Gibco, catalog number: 35050061) and
754 20 ng/mL recombinant mouse GM-CSF (Fujifilm, catalog number: 077-04674).
755 Resuspended cells were plated in sterile culture dishes at a density of 1×10^6
756 cells/mL and cultured at 37 °C in an incubator containing 5 % CO_2. On day 3, the equal
757 volume of the fresh complete medium containing GM-CSF was added to the cultured
758 medium. On day 7, LPS (Sigma, Escherichia coli o55:B5, catalog number: L2880) was
759 applied to the cultured cells at a final concentration of 200 ng/mL to induce dendritic cell
760 maturation. After 18 ~ 24 hours of incubation, non-adherent mature dendritic cells were
761 collected by gently pipetting the medium, and then centrifuged at 190 G for 5 min. The

762 supernatant was discarded, and the pellet was resuspended in the fresh complete medium
763 containing GM-CSF and transferred to new culture dishes. Non-adherent mature dendritic
764 cells were collected from culture dishes and used for following experiments. We also
765 confirmed that shootin1b KO does not affect the expression level of the CCL19 receptor,
766 CCR7 (Figure S2E-F), and those of the dendritic cell markers, CD11c, MHC II and CD80,
767 on dendritic cells (Figure S9).
768
769 **Transfection of dendritic cells**
770 Dendritic cells were transfected with DNA vectors using the NEON electroporation
771 system (Invitrogen, catalog number: MPK5000). On culture day 7, non-adherent cells
772 were washed by PBS and resuspended in 10 μL resuspension buffer R (Invitrogen:
773 catalog number: MPK1025R) at a density of 2.0×10^7 cells/mL. The cells were
774 subsequently mixed with DNA vectors and electroporated by the electroporation system.
775 The transfected cells were plated in the complete RPMI-1640 medium. After more than
776 6h of culture, LPS was applied to the cultured cells at a final concentration of 200 ng/mL
777 to induce dendritic cell maturation.
778
779 **Glioblastoma cell culture and transfection**
780 Human glioblastoma-derived cells (KNBTG-8 cells) were isolated from the tumor
781 specimen of a 74-year-old female patient located in the left occipital lobe using the cell
782 sphere method as previously described[78,79]. This tumor was pathologically diagnosed as
783 glioblastoma, IDH-wildtype CNS WHO grade 4, with *TERT* promoter mutation, *EGFR*
784 gene amplification, *PTEN* deletion, and *CDKN2A/B* deletion. Briefly, brain tumor tissue
785 specimens were mechanically dissociated, digested with 0.05% trypsin-EDTA (Thermo
786 Fisher Scientific, Waltham, MA, USA), and then, cultured as floating culture of cell
787 spheres in the completed DMEM/F12 medium (Sigma, catalog number: H4034),
788 Antibiotic-Antimyotic (1:100 dilution, Thermo, catalog number: 15240062), 20 ng/mL
789 EGF (PeproTech, catalog number: AF-100-15), 20 ng/mL FGF (PeproTech, catalog
790 number: AF-100-18B), 10 ng/mL leukemia inhibitory factor (Millipore, LIF-1010), 2%
791 B27 supplement (Thermo, catalog number: 17504044), and 5 ng/mL heparin (Sigma,
792 catalog number: H3149), as described[78,79]. Half of the medium was changed once per
793 week. The spheres were dissociated into single cells every 2 weeks by incubation with

794 Accutase (Nacalai, catalog number: 12679-54) at 37 °C for 10 min. The cells were then
795 resuspended in 50% fresh medium plus 50% conditioned medium at a density of 1×10^5
796 cells/mL and cultured in culture flasks.
797 Glioblastoma cells were transfected with DNA vectors using the Nucleofector2B
798 electroporation system (Lonza, catalog number: AAB-1001). After dissociation of the
799 cell sphere by Accutase, the cells were washed with PBS and resuspended in 100 μL
800 nucleofector solution (Lonza, catalog number: VPG1004) at a density of 1.0×10^7 cells/mL.
801 They were subsequently mixed with DNA vector and electroporated by Nucleofector2B
802 machine.
803
804 **HEK293T cell and human astrocyte culture and transfection**
805 HEK293T cells (ATCC, catalog number: CRL3216) and primary human brain astrocytes
806 (Applied cell biology, catalog number: ACBRI 371)[80] were cultured in DMEM (Sigma,
807 catalog number: D6429) supplemented with 10% FBS, 100 U/mL Penicillin-100 μg/mL
808 streptomycin, 0.01 % Gentamycin (Gibco, catalog number: 15750060) as described
809 previously[39]. HEK 293T cells were transfected with plasmid DNA using PEI MAX
810 (Polysciences, catalog number: 24765) following the manufacture's protocol.
811
812 **Mouse primary astrocyte cell culture**
813 Primary cultured astrocytes were prepared from the cerebral cortices postnatal day 1 mice
814 as described[81]. They were cultured in Dulbeco's modified Eagle's medium supplemented
815 with 10% FBS, 100 U/mL Penicillin-100 μg/mL streptomycin, and 0.01 % Gentamycin.
816 After two weeks, the cells were grown to a confluent monolayer and used for the
817 immunoblot analysis.
818
819 **Generation of brain cortex organoid derived from human iPS cells**
820 iPSC line B7 (201B7 cell line) were obtained from RIKEN BioResource Research Center
821 and cultured on 0.1% gelain-coated plates with irradiated mouse embryonic feeders
822 (MEF) in Primate ESC Medium (Repro, catalog number: RCHEMD001) supplemented
823 with 10 ng/mL of human basic Fibroblast Growth Factor (FGF, Sigma, catalog number:
824 F0291). They were maintained at 5% CO_2 at 37℃ with daily medium change and were

825 passaged every 6 days at 1:3–1:6 using cell dissociation (CTK) solution (Repro, catalog
826 number: RCHETO002)[82].
827 Cortical organoid differentiation was performed as described[83,84] with several
828 modifications. Briefly, iPSCs were dissociated to single cells and plated into low-
829 attachment V-bottom 96-well plates (Greiner Bio-One, catalog number: 651161) to form
830 aggregates in Glasgow's Minimal Essential Medium (GMEM, Gibco, catalog number:
831 11710035) supplemented with 20% KSR (knockout serum replacement, Gibco, catalog
832 number: 10828010), 1 × MEM-NEAA solution (modified Eagle's medium (MEM) non-
833 essential amino acids solution (Gibco, catalog number: 11140050), 100 μg/mL of
834 Primocin (InvivoGen, catalog number: 14860-94), 0.1 mM 2-Mercaptoethanol (Gibco,
835 catalog number: 21985023), 1 mM Sodium Pyruvate (Gibco, catalog number: 11360070),
836 20 μM ROCK inhibitor (FUJIFILM, catalog number: 036-24023), 3 μM Wnt antagonists
837 (Sigma, catalog number: 681669) and 5 μM TGF-b inhibitor (Tocris, catalog number:
838 1614). Half of the medium was changed every 2–3 days. ROCK inhibitor was removed
839 after 6 days. Aggregates were then transferred to a hyperoxygenated incubator at 5% CO_2
840 and 40% O_2 and maintained in DMEM/F12 supplemented with N2 supplement (Gibco
841 catalog number: 17502048), GlutaMAX (Gibco, catalog number: 35050061), chemically
842 defined lipid concentrate (CDLC, Gibco, catalog number: 11905031), and 0.4%
843 methylcellulose (Sigma, catalog number: M7140). The culture medium was changed
844 every 2–3 days thereafter.
845 On day 35, the organoids were cut in half using Micro Scissors, and the medium
846 was changed to N2B27 medium containing DMEM/F12 supplemented with N2
847 supplement, GlutaMAX, CDLC, 0.4% methylcellulose, B27 without vitamin A (Gibco,
848 catalog number: 12587010), 1% growth factor-reduced Matrigel (Corning, catalog
849 number: 354230), and 5 μg/mL of heparin (Sigma, catalog number:H3149). On day 56,
850 organoids were cut in half and transferred to oxygen permeable dishes containing N2B27
851 medium. Organoids were subsequently cut in half every 2 weeks and routinely sustained
852 for up to 120 days. For STAT3 activation to differentiate and obtain mature cortical
853 organoids, recombinant mouse LIF (Sigma, catalog number: ESG1107) was added at
854 2,000 U/mL from day 35 onward.
855

856 **METHOD DETAILS**

857

858 **DNA construction and RNAi experiment**

859 Preparations of vectors to express pCMV-flag-shootin1b, pFN21A-Halotag-shootin1b,
860 pFN21A-Halotag-actin, pFC14K-L1-HaloTag, pCAGG-myc-shootin1(1-125),
861 pCAGGS-EGFP-shootin1(1-125) have been described have been described
862 previously[39,85]. pEGFP_WT-talin1(1-2541) (mouse talin1 full length WT-EGFP) was a
863 gift from Vesa Hytönen (Addgene plasmid # 166112 ; http://n2t.net/addgene:166112 ;
864 RRID: Addgene 166112)[86].

865 To generate pEGFP-N1-LifeAct vector, the annealed LifeAct (forward: 5′-
866 TCGAGATGGGTGTCGCAGATTTGATCAAGAAATTCGAAAGCATCTCAAAGG
867 AAGAAGGG-3′; reverse: 5′-
868 GATCCCTTCTTCCTTTGAGATGCTTTCGAATTTCTTGATCAAATCTGCGACAC
869 CCATC-3′) was fused to N-terminal of EGFP-N1 vectors (Clontech, catalog number:
870 6085-1).

871 Unphosphorylated (S101A/S249A: AA) and phosphomimic (S101D/S249D:
872 DD) mutants of rat shootin1b[30] were generated with the QuickChange II site -directed
873 mutagenesis kit (Stratagene) to replace each serine (S) with alanine (A) or aspartate (D)
874 using the following primers : S101A Fw (5'-AAAAGAATCGCCATGCTATACATG-
875 3'), S101A Rv (5'-CATGTATAGCATGGCGATTCTTTT-3'), S101D Fw (5'-
876 AAAAGAATCGACATGCTATACATG-3'), S101D Rv (5'-
877 CATGTATAGCATGTCGATTCTTTT-3'), S249A Fw (5'-
878 AAGAGACAAGCCCACCTTCTGCTG-3'), S249A Rv (5'-
879 CAGCAGAAGGTGGGCTTGTCTCTT-3'), S249D Fw (5'-
880 AAGAGACAAGACCACCTTCTGCTG-3'), S249D Rv (5'-
881 CAGCAGAAGGTGGTCTTGTCTCTT-3'). cDNA of shootin1b DD or AA mutants was
882 sub-cloned into pCMV-flag vector[85].

883 To generate AcGFP-integrin β1 and β2 intracellular domains (ICDs), integrin
884 β1- or β2-ICD was amplified mouse brain cDNA (for integrin β1 cDNA) or mouse
885 dendritic cell cDNA (for integrin β2 cDNA) by PCR using the following primers :
886 Integrin β1-ICD Fw (5'-AAAGGATCCAAACTTTTAATGATAATTCAT-3'), Integrin
887 β1-ICD Rv (5'-AAAGTCGACTCATTTTCCCTCATACTTCG-3'), Integrin β2-ICD Fw

888 (5'-AAAGGATCCAAGGCCCTGACCCACCT-3'), Integrin β2-ICD Rv (5'-
889 AAAGTCGACCTAGCTTTCAGCAAACTTGGG-3'). cDNA of integrin β1-, β2-ICD
890 and L1-ICD[39] were subcloned into AcGFP vector (Clontech, catalog number: 632470).
891 For mouse talin1 and human shootin1b RNAi experiments, we used a Block-iT
892 Pol II miR RNAi expression vector kit (Invitrogen, catalog number: K493600) and Block-
893 iT RNAi designer. The targeting sequences for mouse talin1 are following: mouse talin1
894 #1 (5'-CATGATGAGTATTCACTGGTT-3'), #2 (5'-
895 TTAAATCAGGCCGCCACAGAA-3'), #3 (5'-TCACATCAAACACCGAGTACA-3'),
896 #4 (5'-TCCTGGTAGCTTGCAAGGTCA-3') or #5 (5'-
897 GGGCCTCAGATAACCTGGTAA-3'). The targeting sequences for human shootin1b
898 are following: human shootin1b #1 (5'-AAGCAATAGGCGAATATGAAG-3'), #2 (5'-
899 AAGACTTGTCGAGAAAGTGCT-3'), #3 (5'-AAGCTGGGACCAGATGTAATA-3'),
900 #4 (5'-GTCCATGTTAGCTGTAGAAGA-3'), #5 (5'-
901 GCTGGAGAAGGACCTTCGAAA-3') or #6 (5'-AAGTTCCAAGGTTACGTTTCA-
902 3'). The oligonucleotides containing target sequences for mouse talin1 (#1 ~ #5) and
903 human shootin1b (#1~#6) were inserted into the RNAi vector to express microRNAs
904 against the targeting sequences. To confirm the reduction of mouse talin1 and human
905 shootin1b expression, immunoblot was performed using lysates of HEK293T cells
906 transfected with mouse talin1-EGFP (RRID: Addgene 166112) and each of mouse talin1
907 RNAi vector (#1 ~ #5) (Figure S6B) or lysates of HEK293T cells transfected with each
908 of human shootin1b RNAi vector (#1 ~ #6) (Figure S8B).
909
910 **RNAi experiment mediated by infection of lentivirus carrying short hairpin RNA**
911 The lentiviral vectors carrying short hairpin RNA (shRNA) against human shootin1b with
912 EGFP and mCherry (pLKO.1-EGFP and pLKO.1-mCherry) were generated by replacing
913 the gene encoding PuroR in pLKO.1 puro (Addgene Plasmid #8453) with EGFP and
914 mCherry, respectively. The inserted oligonucleotides containing target sequences were
915 designed according to the online cloning protocol of pLKO.1
916 (https://www.addgene.org/protocols/plko/). The target sequences used in this study are as
917 follows: (5'-CCTAAGGTTAAGTCGCCCTCG-3') for a scramble RNA as a negative
918 control, #7 (5'-TGGTCATAGAGGAAGTTAATT-3') and #8 (5'-
919 AAGACTTGTCGAGAAAGTGCT-3') for human shootin1b. The oligos were inserted

920 into pLKO.1-mCherry and pLKO.1-EGFP vectors, yielding to pLKO.1-shScramble-
921 mCherry and pLKO.1-shShootin1b-EGFP to produce lentivirus carrying shRNAs against
922 Scramble (control) and human shootin1b (#7) were used for RNAi experiments in Figure
923 7G-H.
924 For lentiviral production, 6 x 10^6 HEK293FT cells were plated on a 10-cm
925 culture dish for one day prior to transfection in complete DMEM medium (Sigma catalog
926 number: D5796) supplemented with 10% FBS, (catalog number: F7524), 292 μg/mL of
927 L-Glutamine, 100 U/mL of penicillin, and 100 μg/mL of streptomycin (Gibco 10378016).
928 10 μg of pLKO.1 lentiviral vector, 3 μg of psPAX2 (Addgene Plasmid #12260), 1.5 μg
929 of pMD2-VSVG (Addgene Plasmid #12259) and 36 μl of FuGENE HD Transfection
930 Reagent (Promega, catalog number: E2312) were mixed in 350 μl of Opti-MEM (Gibco,
931 catalog number: 31985062) and stored at room temperature for > 15 min before the
932 transfection, and then this mixture was added to the medium of HEK293FT cells. After
933 16 h incubation, the culture medium was replaced with 10 ml of a fresh complete DMEM
934 medium. After 6 hours, the culture medium was further replaced with 4 ml of the optimal
935 culture medium for glioblastoma cells. The 4 mL of viral supernatant was collected every
936 24 hours followed by the addition of 4 mL of the fresh optimal glioblastoma cell culture
937 medium. The collected supernatant (total 8 mL) was filtered by 0.45 μm filter (Millipore,
938 catalog number: SLHPR33RS).
939 For lentivirus infection to glioblastoma cells, the viral supernatant was added to
940 the culture medium. Twenty four hours after the infection, the virus-containing medium
941 was replaced with a fresh medium. Expression of mCherry and EGFP (pLKO.1-
942 shScramble-mCherry and pLKO.1-shShootin1b-EGFP) was confirmed within 48 h after
943 infection under an epifluorescent microscopy. Successful reduction of shootin1b
944 expression level was validated by immunoblotting using the lysates of the infected
945 glioblastoma cells (shootin1b RNAi #7, #8) (Figure S8C).
946
947 **Invasion assay using brain cortex organoid**
948 Tumor spheroids were formed by mixing glioblastoma cells expressing shScramble-
949 mCherry or shShootin1b-EGFP in a 1:1 ratio (1.5×10^4 cells), followed by 72 h
950 incubation in a V-bottom 96-well plate (Greiner, catalog number: 651101) at 37 °C, 5%
951 CO_2. Then, the tumor spheroids were co-cultured with the brain cortex organoid for an

952 additional 72 h at 37 °C, 5% CO_2 to allow fusion between the spheroids and organoids in
953 N2B27 organoid culture medium. mCherry- or EGFP-labelled glioblastoma cells invaded
954 from the spheroids to the organoids. Five days after fusion between the spheroids and
955 organoids, they were fixed by 4% Paraformaldehyde in PBS for 40 minutes on ice, and
956 then washed twice in PBS. The fixed organoids were then cryo-preserved in 30% sucrose
957 in PBS overnight at 4 °C until completely submersed and embedded in OCT-compound
958 blocks. Subsequently, the organoids were cryo-sectioned at 10μm thickness, and collected
959 onto Superfrost Plus slides (Fisher Scientific, catalog number: 1255015). Nuclei were
960 stained with DAPI for 5 min before mounting slides with Prolong Antifade Mountant
961 (Invitrogen, catalog number: P36970).
962 Fluorescence images were obtained by an Olympus FV3000 microscope
963 equipped with ×20 and ×40 dry objectives. All images were compiled in ImageJ and
964 Adobe Photoshop, with image adjustments applied to the entire image and restricted to
965 brightness, contrast, and levels. Images shown in figures were obtained and processed in
966 parallel using identical imaging settings. To quantify the distribution of infected tumor
967 cells, the invasion distance from the spheroid to the organoid was first measured in the
968 slice of tumor-spheroid-fused organoid. Then, the ratio of the number of shScramble cells
969 or shShootin1b cells invaded in the organoid at each range of 0~100 μm, 100~200 μm, or
970 200~300 μm to the number of total cells (shScramble cells or shShootin1b cells) was
971 calculated.
972
973 **Flow cytometry analysis**
974 Non-adherent mature dendritic cells were collected and washed with PBS. The cells were
975 then resuspended in HBSS without Ca^{2+} buffer (Gibco, catalog number: 14175-095)
976 containing 2 mM EDTA and 1% BSA at a density of 1×10^6 cells/mL. For Fc receptor
977 blocking, anti-mouse CD16/CD32 antibody (BD Biosciences, catalog number: 553142)
978 was added to the cell suspension at 1:500 dilution at 4°C to prevent non-specific antibody
979 binding. After 30 min, the cells were washed with PBS and resuspended in the buffer at
980 4°C. To analyze the cell surface markers of mature dendritic, the cells were stained for
981 30 min at 4°C by the following antibodies; anti-mouse CD11c-FITC (1:500 dilution)
982 (Miltenyi, catalog number: 130-110-837), anti-mouse-MHCII-FITC (1:500 dilution)
983 (Miltenyi, catalog number: 130-112-386), and anti-mouse-CD80-FITC (1:500 dilution)

984 (Miltenyi, catalog number: 130-116-459) antibodies. The anti-IgG REA-FITC antibody
985 (1:500 dilution) (Miltenyi, catalog number: 130-113-449) was used as an isotype IgG
986 control antibody for negative staining. The stained cells were washed with PBS and
987 resuspended in the HBSS without Ca^{2+} buffer at a density of 1×10^6 cells/mL. The cell
988 suspension was filtrated by 35 μm cell strainer cap with a 5 mL tube (Falcon, catalog
989 number: 352235) to remove the aggregated cells, and then loaded into the MA900 flow
990 cytometer (Sony, catalog number: P1FFW1000040-1) for the analysis of the dendritic
991 cell surface markers. The percentage of dendritic cell surface marker positive cells were
992 calculated using Cell Sorter Software (Sony). The range of negative cells was determined
993 using the isotype IgG control antibody (see magenta frame in Figure S9A). More than
994 90 % of the cells were positive for the mature dendritic cell markers in WT and shootin1b
995 KO cells (see green frames in Figure S9B-D).
996
997 **Immunocytochemistry**
998 Dendritic cells and glioblastoma cells were fixed with 3.7 % formaldehyde in PBS for 10
999 min at room temperature and for 5 min on ice, followed by treatment with 0.05% Triton
1000 X-100 in PBS for 15 min on ice and 10 % FBS in PBS for 1 hour at room temperature.
1001 They were then incubated overnight at 4°C with primary antibodies diluted in PBS
1002 containing 10% FBS. The following primary antibodies were used: rabbit anti-shootin1b
1003 (1:2000 dilution), rabbit anti-shootin1a (1:2000 dilution), rabbit anti-pSer249 (1:1000
1004 dilution), mouse anti-cortactin (1:500 dilution) (Millipore, catalog number: 05-180),
1005 mouse anti-L1 (1:500 dilution) (Santa Cruz, catalog number: sc-514360), mouse anti-myc
1006 (1:1000) (MBL, catalog number: 562-5), and Armenian hamster anti-CD11c (1:400
1007 dilution) (BD Biosciences, catalog number: 550283) antibodies. The cells were washed
1008 with PBS, and then incubated with secondary antibodies diluted in PBS for 1 hour at room
1009 temperature. The following secondary antibodies were used: Alexa Fluor 488 conjugated
1010 goat anti-rabbit (1:1000 dilution) (Thermo Fisher, catalog number: A11008), TRITC
1011 conjugated goat anti-rabbit (1:1000 dilution) (Thermo Fisher, catalog number: A16101),
1012 Alexa Fluor 594 conjugated goat anti-mouse (1:1000 dilution) (Invitrogen, catalog
1013 number: A11032), Alexa Fluor 488 conjugated goat anti-mouse (1:1000 dilution)
1014 (Invitrogen, catalog number: A11029) and Alexa Fluor 594 conjugated goat anti-
1015 Armenian hamster (1:1000 dilution) (Jackson ImmunoResearch, catalog number: 127-

1016 585-160) antibodies. For F-actin staining, cells were stained with Alexa Fluor 555
1017 conjugated phalloidin (1:100 dilution) (Cell Signaling, catalog number: 8953) for 30 min
1018 at room temperature. Immunostained cells were mounted with 50% (v/v) glycerol in PBS
1019 for a fluorescence microscope or ProLong Gold (Thermo Fisher, catalog number:
1020 P36930) for a Leica Stellaris 8 STED microscope.
1021 Fluorescence images were acquired using a fluorescence microscope (BZ-X710,
1022 KEYENCE) equipped with a UPlansApo 60 × oil, 1.35 NA objective (Olympus), a Plan-
1023 Apochromat 100 × oil, 1.45 NA objective（KEYENCE) and imaging software (BZ-X
1024 Analyzer software) (BZH4A, KEYENCE) or a Leica Stellaris 8 STED microscope
1025 equipped with an HC PL APO 93×/1.30-motCORR glycerol immersion objective lens
1026 and imaging software (LAS X) (Leica Microsystems). ProLong Gold was used as
1027 mounting agent for STED image acquisition. Dendritic cell images were acquired with
1028 x/y pixel size of 41 or 68 nm for the whole cell (left panels in Figures 1F and S2C-D) and
1029 15 or 24 nm for the leading edge (right panels in Figures 1F and S2C-D). Glioblastoma
1030 cell images (Figure 6B) were acquired with x/y pixel size of 41 nm for the whole cell and
1031 12 nm for the tip of the tumor microtube. Stimulated emission depletion was
1032 accomplished with a 660 nm STED laser. Excitation was provided by a white light laser
1033 at the desired wavelength for each sample.
1034
1035 **Immunoprecipitation and Immunoblot**
1036 Immunoprecipitation and immunoblot were performed as described[26,39]. For
1037 immunoprecipitation with dendritic cells after stimulation with CCL19 (0, 20, 200
1038 ng/mL) (R&D Systems, catalog number: 440-M3-025) for 30 min (Figure 3C) and
1039 HEK293T cells expressing AcGFP-tagged proteins and flag-shootin1b (Figure S6A), cell
1040 lysates were collected by NP40-Triton lysis buffer (0.5% NP-40, 0.5% Triton X-100, 20
1041 mM HEPES pH 7.5, 3 mM MgCl2, 100 mM NaCl, 1 mM EGTA, 1 mM DTT, 1 mM
1042 PMSF, 0.01 mM leupeptin, 1× PhosStop). The supernatants of the lysates were incubated
1043 with anti-shootin1 antibody (Figure 3C) or anti-flag antibody (Sigma, catalog number:
1044 F3165) (Figure S6A) overnight at 4°C, and then the immunocomplexes were precipitated
1045 with protein G-sepharose 4 (GE Healthcare, catalog number: 17061801). After washing
1046 the beads with wash buffer (0.1% Tween 20, 20 mM HEPES pH 7.5, 3 mM MgCl2, 100

1047 mM NaCl, 1 mM EGTA, 1 mM DTT), the immunocomplexes were detected by
1048 immunoblot using rabbit anti-shootin1b (1:5000 dilution), mouse anti-cortactin (1:1000
1049 dilution), mouse anti-L1 (1:1000 dilution), rabbit anti-GFP (1:1000 dilution) (MBL,
1050 catalog number: 598) and rabbit anti-flag antibodies (1:1000 dilution) (MBL, catalog
1051 number: PM020).

1052 To determine shootin1b phosphorylation, dendritic cells were incubated with
1053 200 ng/mL CCL19 (R&D Systems, catalog number: 440-M3-025) at each time point (0,
1054 10, 30, 60 min) (Figure S4A) or each CCL19 concentration (0, 20, 200, 2000 ng/mL) for
1055 30 min (Figure 3A). To analyze Pak1-mediated shootin1b phosphorylation (Figure S4C),
1056 mature dendritic cells were incubated with 0.1 % BSA (control), 200 ng/mL CCL19 or
1057 200 ng/mL CCL19 + 250 nM NVS-Pak1-1 (Pak1 inhibitor) (Sigma, catalog number:
1058 SML1867-5MG). Dendritic cell lysates were collected using RIPA buffer (50 mM Tris-
1059 HCl pH8.0, 150 mM NaCl, 1 mM EDTA, 1% Triton, 0.1% SDS, 0.1% sodium
1060 deoxycholate, 1 mM DTT, 1 mM PMSF, 0.01 mM leupeptin, 1× PhosStop). Immunoblot
1061 was performed using rabbit anti-pSer101-shootin1 (1:1000 dilution), rabbit anti-pSer249-
1062 shootin1 (1:2000 dilution) and rabbit shootin1b (1:5000 dilution) antibodies as
1063 described[39]. For the mouse talin1 and human shootin1b RNAi experiments (Figures S6B,
1064 S8B), HEK293T cells were transfected with talin1-EGFP + talin1 RNAi vector or
1065 shootin1b RNAi vector using PEI MAX. After 48 hours, lysates of the transfected cell
1066 were collected by RIPA buffer. Immunoblot was performed using mouse anti-GFP
1067 (1:1000 dilution) (MBL, catalog number: M048-3), mouse anti-actin (1:5000 dilution)
1068 (Millipore, catalog number: MAB1501) and rabbit anti-shootin1b (1:5000 dilution)
1069 antibodies. To analyze the expression of shootin1b, shootin1a, cortactin, L1 and CCR7 in
1070 mature dendritic cells, glioblastoma cells and human astrocytes, the cell lysates were
1071 collected by RIPA buffer. Immunoblot was performed using rabbit anti-shootin1b
1072 (1:5000), rabbit anti-shootin1a (1:5000), mouse anti-cortactin (1:1000 dilution), mouse
1073 anti-L1 (1:1000 dilution) and rabbit anti-CCR7 (1:4000) antibodies.
1074

1075 **Chemotaxis assay and random migration assay**

1076 To accurately track migrating dendritic cells, the nuclei of cells were stained with Hoechst
1077 (1:2000 dilution) (Thermo Fisher, catalog number R37605) for 30 min in the serum-free
1078 complete RPMI-1640 medium. For the chemotaxis assay, dendritic cells (1×10^5 cells)

1079 were embedded in the 100 μL mixture of 1.5 mg/mL collagen gel (bovine collagen type
1080 I) (KOKEN, catalog number: IAC-50) + 10 % Matrigel (Corning, catalog number:
1081 356231) mixed to give the compositions listed in Table S1. Matrigel was used to allow
1082 laminin-mediated migration in collagen gel[47]. The cell mixture was placed in a μ-slide
1083 chemotaxis chamber (Ibidi, catalog number: ib80326) according to the manufacturer's
1084 instructions and incubated at 37 °C, 5 % CO_2 for 30 min to allow polymerization of
1085 collagen fibers and gelation of Matrigel. 600 ng/mL CCL19[11] (R&D Systems, catalog
1086 number: 440-M3-025) in 10% FBS/RPMI-1640 was added to the CCL19 source side of
1087 the reservoir, while 10 % FBS/RPMI-1640 medium (chemoattractant-free medium) was
1088 added to the opposite side.

1089 For the random migration assay under the bath application of CCL19, dendritic
1090 cells (5×10^4 cells) were embedded in the 100 μL mixture of 1.5 mg/mL collagen gel +
1091 10 % Matrigel + CCL19 (20 or 200 ng/mL) mixed to give the compositions listed in Table
1092 S1. The cell-mixture was placed on the glass bottom dish (Matsunami, catalog number:
1093 D11130H). After 30 min incubation to allow polymerization of collagen fibers and
1094 gelation of Matrigel, the surface of the mixture was covered with the complete RPMI1640
1095 medium including CCL19 (20 or 200 ng/mL). Time-lapse images were acquired every 1
1096 min for 180 min at 37 °C using a fluorescence microscope (IX81, Olympus) equipped
1097 with an EM-CCD (Ixon DU888, Andor), a Plan Fluor × 20, 0.45 NA objective (Olympus)
1098 and MetaMorph software. Migrating cells were tracked using the manual tracking (Fiji)
1099 to calculate migration speed and the chemotaxis index (straight distance toward the
1100 CCL19 source/total distance) (Figure 4C).

1101

1102 **Glioblastoma cell and astrocyte 3D migration assay**

1103 Glioblastoma cells or human astrocytes were embedded in 50 % Matrigel diluted with the
1104 complete DMEM/F12 medium at a density of 5×10^5 cells/mL. The Matrigel-cell mixture
1105 was placed on the glass bottom dish (Matsunami, catalog number: D11130H), and then
1106 this mixture was incubated for 30 min at 37 °C, 5 % CO_2 to allow gelation of Matrigel.
1107 The surface of the mixture was covered with complete L15 medium (Gibco, catalog
1108 number: 21083027) supplemented with Antibiotic-Antimyotic (1:100 dilution), 20 ng/mL
1109 EGF, 20 ng/mL FGF, 10 ng/mL leukemia inhibitory factor, 2% B27 supplement and 5
1110 ng/mL heparin + conditioned medium in a 1:1 ratio. After 24h of culture, time-lapse

1111 images were acquired every 10 min for 480 min at 37 °C using a fluorescence microscope
1112 (IX81, Olympus) equipped with an EM-CCD (Ixon DU888, Andor), a Plan Fluor × 20,
1113 0.45 NA objective (Olympus), and MetaMorph software.
1114
1115 **Fluorescent speckle imaging**
1116 Fluorescent speckle imaging was performed as previously described[31] with modifications.
1117 Dendritic cells or glioblastoma cells were treated with TMR ligand (Promega, catalog
1118 number: G299A) at 1:2000 (final concentration 50 nM) in the serum-free complete
1119 RPMI-1640 medium (for dendritic cells) or the serum-free complete DMEM/F12 medium
1120 (for glioblastoma cells) for 30 min at 37 °C, 5 % CO_2 to visualize HaloTag-actin,
1121 HaloTag-shootin1b or Halotag-L1. The ligand was then washed with PBS, and cells were
1122 incubated in the complete RPMI-1640 medium or the complete DMEM/F12 medium at
1123 37 °C, 5 % CO_2.
1124 For fluorescent speckle imaging in dendritic cells, a 1 % agarose block was
1125 prepared by mixing the following in a 1:2:1 ratio : (i) 56 °C pre-warmed 2×HBSS (Sigma,
1126 catalog number: H-1387), (ii) 56 °C pre-warmed RPMI-1640 medium supplemented with
1127 20 % FBS, (iii) 4 % agarose (Sigma, catalog number: 16500) in warmed water.
1128 Recombinant mouse CCL19 (20 ng/mL or 200 ng/mL) (R&D Systems, catalog number:
1129 440-M3-025) was added to liquid agarose when liquid agarose was heated to 37 °C. The
1130 liquid agarose was then poured into a glass bottom dish coated with PDL (Sigma, catalog
1131 number: P6407) and laminin (Fujifilm, catalog number: 120-05751) and allowed to
1132 solidify for 1 hour at room temperature. After the TMR treatment and PBS washing,
1133 dendritic cells were resuspended in the complete RPMI1640 medium containing CCL19
1134 (20 or 200 ng/mL) at a density of 1×10^6 cells/mL. The cell suspension of the cells was
1135 injected under the agarose block on the laminin-coated glass bottom dish. For fluorescent
1136 speckle imaging in glioblastoma cells, 1×10^5 glioblastoma cells were placed on the glass
1137 bottom dish coated subsequently by PDL and laminin. After the TMR treatment and PBS
1138 washing, the medium was changed to 50% conditioned medium + 50% the complete L15
1139 medium.
1140 Fluorescent speckles were observed at the leading edge of dendritic cells and at
1141 the tip of the tumor microtube of glioblastoma cells at 37 °C using a TIRF microscope
1142 (IX81; Olympus) equipped with an EM-CCD (Ixon3, Andor), a complementary metal

1143 oxide semiconductor (CMOS) camera (ORCA Flash 4.0LT, HAMAMATSU), a UAPON
1144 ×100 1.49 NA (Olympus) and MetaMorph software[87] for dendritic cells, or using a
1145 fluorescence microscope (AxioObserver Z1, Carl Zeiss) equipped with a complementary
1146 metal oxide semiconductor (CMOS, ORCA Flash4.0 V2, Hamamatsu), a Plan-
1147 Apochromat 100x, 1.40 NA (Carl Zeiss), and imaging software (ZEN2012, Carl Zeiss)
1148 for glioblastoma cells[31]. Fluorescence time-lapse images were acquired every 2 sec for
1149 dendritic cells and 5 sec for glioblastoma cells. We analyzed the fluorescent speckles that
1150 could be traced for at least 5 frames during imaging. F-actin flow velocity was calculated
1151 by tracing the speckle of HaloTag-actin. Actin polymerization rate was calculated as the
1152 sum of the F-actin retrograde flow and extension rates as reported[31].
1153
1154 **Traction force microscopy**
1155 Traction force microscopy was performed as previously described[31] with modifications.
1156 Polyacrylamide gels with embedded fluorescent nano beads (200 nm diameter) (Thermo,
1157 catalog number: F8810) were prepared as described[31]. To measure forces under dendritic
1158 cells, they were stained for 30 min by 1 μM CMFDA (Invitrogen, catalog number: C2925)
1159 in serum-free complete RPMI-1640 medium, or transfected with EGFP or EGFP-
1160 shootin1-DN (dominant negative shootin1)[39] to visualize the entire cell body. CMFDA-
1161 or EGFP-labeled dendritic cells (1×10^5 cells) were placed on the PDL- and laminin-
1162 coated polyacrylamide gels for 30 min at 37 °C, 5 % CO_2 to allow the adhesion to the
1163 gels. Cells were covered by the mixture of 1.5 mg/mL collagen gel + 10% Matrigel +
1164 CCL19 (20 or 200 ng/mL). The mixture was incubated at 37 °C, 5 % CO_2 for 30 min to
1165 allow polymerization of collagen fibers and gelation of Matrigel. To measure forces under
1166 glioblastoma cells, they were transfected with human shootin1b RNAi vector to co-
1167 express microRNA against human shootin1b RNA target sequence and EGFP to visualize
1168 the entire cell body. EGFP-labeled glioblastoma cells (1×10^5 cells) were cultured
1169 overnight on the PDL- and laminin-coated polyacrylamide gels.
1170 Time-lapse imaging of fluorescent nano beads and cells was performed at 37 °C
1171 using confocal microscope (LSM 710, Carl Zeiss) equipped with a C-Apochromat
1172 63×/1.2 W Corr objective. Time-lapse images were acquired every 3 sec. The leading
1173 edge of a dendritic cell or the tumor microtube of a glioblastoma cell was determined by
1174 CMFDA or EGFP fluorescence images and DIC images. Traction forces under the cells

1175 were monitored by visualizing the force-induced deformation of the elastic substrate,
1176 which is reflected by the movement of the beads from their original positions[31]. The force
1177 vectors detected by beads under individual dendritic cells or under the tip of the tumor
1178 microtube of glioblastoma cells were then averaged, and were expressed as a vector
1179 composed of magnitude and angle (θ).
1180
1181 **Analysis of the correlation between the directions of force and cell migration**
1182 To analyze a possible correlation between the direction of traction force and the direction
1183 of dendritic cell migration, the 90 time-lapse images taken every 3 sec for 270 sec (Figure
1184 1B) were divided into 3 groups: 1-90 sec (30 images), 91-180 sec (30 images), and 181-
1185 270 sec (30 images). The angle of the traction force was calculated for each image as
1186 described above, and then the average angle of the 30 images during the 90-sec
1187 observation in each group ($\theta 1$) was determined. The centroid of migrating cells in each
1188 image was calculated from the manually traced cell contour using Image J (Fiji), then the
1189 direction of cell migration during 90-sec observation in each group ($\theta 2$) was determined
1190 by the locations of the centroids in the 1st and 30th images. Thus, the 36 data in Figure
1191 1E correspond to data from 12 cells (3 data from each cell).
1192
1193 **Analysis of dendritic cell migration in lymph node slice**
1194 Live imaging of dendritic cells in lymph node slices was performed as described[88,89] with
1195 modifications. Isolated lymph nodes (inguinal, axial) were embedded in 4 % low gelling-
1196 temperature agarose (Sigma, catalog number: A0701) diluted in PBS. Agar-embedded
1197 lymph node tissue was sliced at 320 μm thickness using a vibratome (Leica) in a bath of
1198 ice-cold PBS. Lymph node slices were placed in a 35 mm culture dish containing the
1199 IMDM medium supplemented with 25mM HEPES, 10 % FBS, 100 U/mL Penicillin-100
1200 μg/mL streptomycin, and then incubated at 37 ℃, 5 % CO_2. WT and shootin1b KO
1201 dendritic cells were labeled with 1 μM CMFDA and 1 μM CMTPX, respectively, in
1202 serum-free complete RPMI-1640 medium for 30 min at 37 ℃, 5 % CO_2. After washing
1203 with PBS, WT and shootin1b KO dendritic cells were resuspended in a 1:1 ratio (WT :
1204 KO) of 1×10^6 cells/mL in the complete RPMI1640 medium. 100 μL of the mixed cell
1205 suspension was placed on the surface of a lymph node slice. The lymph node slice with
1206 cells was incubated at for 60 min at 37 ℃, 5 % CO_2 to allow dendritic cell migration into

1207 the lymph node slice. After washing with PBS to remove the cells that did not migrate
1208 into the tissue, the lymph node slice was placed in glass bottom dish containing the
1209 complete RPMI1640 medium.

1210 Dendritic cells in the lymph node slice were observed using a Leica SP8 Falcon
1211 microscope equipped with an HC PL APO 20×/0.75 dry objective lens and imaging
1212 software (LAS X) (Leica Microsystems). Fluorescence images were collected at more
1213 than 10 ~ 25 μm below the surface of the lymph node slice. Fluorescence time-lapse
1214 images of x-y section with 10 μm z-spacing in total depth of 40 ~ 50 μm were acquired
1215 at 37 °C every 30 sec for 60 min. In our perfusion system, a glass bottom dish containing
1216 the lymph node slice was placed in a custom chamber, and the oxygenated fresh
1217 RPMI1640 medium was delivered into the dish from one side using a peristaltic pump
1218 (ATTA, catalog number: SJ-1211) at a rate of 0.5 mL/min. The ascending medium was
1219 aspirated using another peristaltic pump connected to a waste collection flask. Thus, the
1220 medium in the glass bottom dish was continuously perfused with fresh RPMI1640
1221 medium oxygenated with 95% O_2・5% CO_2 gas at 37°C during time-lapse imaging.

1222

1223 ***In vivo* dendritic cell migration assay.**

1224 WT and shootin1b KO dendritic cells were labeled with 1 μM CMTPX and 1 μM
1225 CMFDA , respectively, in serum-free RPMI1640 medium for 60 min. After washing with
1226 PBS, 3×10^6 dendritic cells in a 1:1 ratio (WT:KO) were suspended in PBS and injected
1227 subcutaneously into the hind footpads of six-week-old C57BL/6 mice. Popliteal lymph
1228 nodes were removed after 24 hours and fixed by immersion in freshly prepared 4%
1229 paraformaldehyde at 4°C for 60 min and frozen in OCT compound (SFJ, catalog number:
1230 4583). 12-μm cryosections cut by a cryostat (Leica) were preincubated with 10 % normal
1231 goat serum (Vector, catalog number: S-1000) in phosphate buffer (PB) containing 0.3 %
1232 Triton-X 100 for 2 hours. The sections were then incubated with anti-pan-laminin
1233 antibody (from rabbit, 1:500 dilution) (Sigma, catalog number: L9393) diluted in PB
1234 containing 0.3 % Triton-X 100 at 4°C overnight. Alexa 647 conjugated donkey anti-rabbit
1235 antibody (Abcam, catalog number: ab150075) was used as secondary antibody at a 1000-
1236 fold dilution overnight at 4°C. The sections were mounted with 50% (v/v) glycerol in PB.
1237 Fluorescence images were acquired using a confocal microscope (LSM710) equipped

1238 with a Plan-Apochromat ×10, 0.45 NA objective lens (Carl Zeiss). The lymph node was
1239 visualized with anti-pan-laminin antibody (Figure 5H). The ratio of WT or shootin1b KO
1240 dendritic cells migrated into the lymph node was calculated as the number of WT or KO
1241 cells divided by the total number of dendritic cells (WT + KO cells) in the T cell cortex
1242 of the lymph node. The average value of the ratio was calculated from three different
1243 layers of 12 μm cryosections in each experiment.
1244

1245 **Generation of CCL19 gradients for immunocytochemistry**

1246 A microfluidic device to generate CCL19 gradients in culture medium was fabricated as
1247 described[90]. Briefly, the device was fabricated with polydimethylsiloxane (PDMS; Silpot
1248 184, Dow Corning Toray, catalog number: 3255981) and attached to a glass coverslip.
1249 The device consists of an open rectangular cell culture area and two microchannels on the
1250 long sides of the culture area. The micro-molds of the channel pattern were
1251 lithographically fabricated on a photoresist (SU-8 3025, MicroChem, USA) spin-coated
1252 on a 70-μm thick silicon wafer. PDMS sheets were obtained from this mold, which had
1253 been treated with silicone oil (Barrier coat No. 6, ShinEtsu, Japan) to facilitate their
1254 removal. The PDMS sheet was then bonded to a glass coverslip using plasma irradiation
1255 (Sakigake, catalog number: YHS-R). The glass coverslip was coated with PDL and
1256 laminin, and then dendritic cells were cultured on the 2-D cell culture area of the device
1257 for 1h to allow adhesion to the laminin-coated glass. To generate CCL19 gradient in the
1258 cell culture area, flow of complete RPMI1640 medium (7.5 μm/min) with or without 600
1259 ng/mL CCL19[11] were applied to the microchannels on either side of the cell culture area
1260 for 30 min using syringe pump.
1261

1262 **QUANTIFICATION AND STATISTICAL ANALYSIS**

1263 All statistical analysis were performed using Microsoft Excel (Microsoft Office LTSC
1264 professional Plus 2021 ver.) and Graphpad prism 7 (GraphPad Software). For samples
1265 with more than 7 data points, the D′Agostino–Pearson normality test was used to
1266 determine whether the data followed a normal distribution. In cases where the number of
1267 data points was between 3 and 7, the Shapiro–Wilk test was used for the normality test.
1268 We also tested the equality of variation with the F-test for two independent groups that
1269 followed normal distributions. Significance tests were performed as follows: (1) two-

tailed unpaired Student′s *t*-test to compare normally distributed data with equal variance from two independent groups; (2) two-tailed unpaired Welch′s *t*-test to compare normally distributed data with unequal variance from two independent groups; (3) two-tailed Mann–Whitney *U*-test to compare nonnormally distributed data from two independent groups. (4) For multiple comparisons, we used one-way ANOVA with Tukey's post hoc test. For each experiment, the corresponding statistical information and number of samples are indicated in the figure legends. For detailed statistical results including the test statistics and p values, see the statistical source data associated with each figure. All data are shown as the mean ± SEM. Statistical significance was defined as ***$p < 0.01$; **$p < 0.02$; *$p < 0.05$; ns, not significant. All experiments were performed at least three times and reliably reproduced. Investigators were blinded to the experimental groups for each analysis, except biochemical analysis.

1282 **Figure Legends**

1283 **Figure 1. Shootin1b mediates generation of weak forces for dendritic cell migration**

1284 (A) Schema of traction force microscopy in a semi-3D condition. Dendritic cells were
1285 cultured on laminin-coated polyacrylamide gels embedded with 200-nm fluorescent
1286 beads in a mixture of collagen gel and Matrigel. Traction force under the cells was
1287 monitored by visualizing force-induced deformation of the gel, which is reflected by the
1288 bead movement (red arrows).

1289 (B) Overlayed differential interface contrast (DIC) and fluorescence images showing a
1290 dendritic cell migrating under the semi-3D condition in (A) in the presence of 200 ng/mL
1291 CCL19. See Video S1. The pictures show representative images from the time-lapse series
1292 taken every 3 sec for 270 sec. The original and displaced positions of the beads in the gel
1293 are indicated by green and red colors, respectively. The cells were visualized by CMFDA
1294 staining (blue color); dashed lines indicate the boundaries of the cells. The kymographs
1295 (panel below) along the axis of bead displacement (white dashed arrows) at indicated
1296 areas 1 and 2 show movement of beads recorded by every 3 sec. The bead in area 2 is a
1297 reference bead. Scale bar: 5 μm (in the inset, 1 μm).

1298 (C) Analyses of the magnitude of the traction force under WT and shootin1b KO
1299 dendritic cells stimulated by 20 ng/mL and 200 ng/mL CCL19. For multiple comparisons,
1300 one-way ANOVA with Turkey's post hoc test was performed. WT + 20 ng/mL CCL19, n
1301 = 12 cells; WT + 200 ng/mL CCL19, n = 12 cells; KO + 20 ng/mL CCL19, n = 12 cells;
1302 KO + 200 ng/ mL CCL19, n = 12 cells.

1303 (D) Analyses of migration speed of WT and shootin1b KO dendritic cells cultured in a
1304 mixture of collagen gel and Matrigel in the presence of 20 ng/mL and 200 ng/mL CCL19.
1305 For multiple comparisons, one-way ANOVA with Turkey's post hoc test was performed.
1306 WT + 20 ng/ mL CCL19, n = 111 cells; WT + 200 ng/ mL CCL19, n = 137 cells; KO +
1307 20 ng/ mL CCL19, n = 107 cells; KO + 200 ng/ mL CCL19, n = 110 cells. See Figures
1308 S1, and Video S2.

1309 (E) Scheme showing the angles of traction force ($\theta 1$) and dendritic cell migration ($\theta 2$)
1310 (left panel). The angles were calculated from the data of sequential 30 images of migrating
1311 dendritic cells in the presence of 200 ng/mL CCL19 (B). Right panel shows the
1312 correlation analysis between the traction force angle and migration angle of dendritic cells.

1313 (F) Fluorescence images of a dendritic cell co-stained with anti-shootin1b antibody and
1314 phalloidin-Alexa 555 for F-actin. An enlarged view of the rectangular region is shown to
1315 the right. Arrowheads indicate shootin1b co-localization with F-actins in filopodia. The
1316 images were obtained by STED microscopy. Scale bar: 10 μm (in the inset, 2 μm).

1317 (G) Overlayed DIC and fluorescence images showing a shootin1b KO dendritic cell

1318 migrating under the semi-3D condition in (A) in the presence of 200 ng/mL CCL19. For
1319 detailed explanations, see (B). See Video S1.
1320 (H, I) Effects of shootin1b KO on the traction force (H) and migration speed (I) increased
1321 by 200 ng/mL CCL19. Two-tailed unpaired Student′s *t*-test was performed (n = 3
1322 independent experiments).
1323 Data represent means ± SEM; **, $p < 0.02$; ***, $p < 0.01$; ns, not significant.
1324
1325 **Figure 2. L1 forms a slippery adhesion-clutch enhanced by laminin**
1326 (A-C) Fluorescent speckle images of HaloTag-actin (A), Halotag-shootin1b (B) and L1-
1327 halotag (C) in dendritic cells cultured on dishes subsequently coated with PDL and
1328 laminin under agarose in the presence of 200 ng/mL CCL19. See Video S6. Time-lapse
1329 montages of the indicated rectangular regions at 2 sec intervals are shown to the right
1330 panel; dashed lines indicate the retrograde flow of speckles. Scale bar: 10 μm (in the inset,
1331 2 μm).
1332 (D) Analyses of the retrograde flow speeds of actin, shootin1b and L1 in (A-C and F-H).
1333 Two-tailed unpaired Welch's *t*-test for Halotag-actin between PDL+laminin- and PDL-
1334 coated dishes. PDL+laminin, n = 55 speckles from 12 cells; PDL, n = 50 speckles from 9
1335 cells. Two-tailed Mann–Whitney *U*-test for Halotag-shootin1b between PDL+laminin-
1336 and PDL-coated dishs. PDL+laminin, n = 48 speckles from 8 cells; PDL, n = 44 speckles
1337 from 7 cells. Two-tailed Mann–Whitney *U*-test for L1-halotag between PDL+laminin-
1338 and PDL-coated dishs. PDL+laminin, n = 44 speckles from 7 cells; PDL, n = 40 speckles
1339 from 6 cells. For multiple comparisons of actin, shootin1b and L1 flow speeds on
1340 PDL+laminin-coated dish (blue dots) or PDL-coated dish (red dot), one-way ANOVA
1341 with Turkey's post hoc test was performed.
1342 (E) Schema of the L1- and shootin1b-mediated slippery adhesion-clutch enhanced by
1343 laminin.
1344 (F-H) Fluorescent speckle images of HaloTag-actin (F), Halotag-shootin1b (G) and L1-
1345 halotag (H) in dendritic cells cultured on PDL-coated dishes under agarose in the presence
1346 of 200 ng/mL CCL19. See Video S6. Time-lapse montages of the indicated rectangular
1347 regions at 2 sec intervals are shown to the right panel; dashed lines indicate the retrograde
1348 flow of speckles. Scale bar: 10 μm (in the inset, 2 μm).
1349 Data represent means ± SEM; ***, $p < 0.01$; ns, not significant.
1350
1351 **Figure 3. CCL19 promotes shootin1b-mediated adhesion-clutch**
1352 (A) Dendritic cells were treated with 0, 20, 200 or 2000 ng/mL CCL19 for 30 min. Cell
1353 lysates were then analyzed by immunoblot with anti-pSer101 shootin1, anti-pSer249

shootin1 and anti-shootin1b antibodies.
(B) Fold change of the phosphorylated shootin1b levels at Ser101 and Ser249 normalized by total shootin1b in (A). One-way ANOVA with Turkey's post hoc test was performed for multiple comparison of the data (n = 3 independent experiments).
(C) Co-immunoprecipitation of L1 and cortactin with shootin1b in dendritic cells. After incubation of dendritic cells with 20 ng/mL, 200 ng/mL CCL19, or medium (0 ng/mL CCL19) for 30 min, cell lysates were prepared and incubated with anti-shootin1 antibody or isotype control IgG for immunoprecipitation. The immunoprecipitates and cell lysates (0.1 %) were immunoblotted with anti-shootin1b, anti-L1, and anti-cortactin antibodies.
(D) Quantitative data for L1 and cortactin co-precipitated with shootin1b in (C). Two-tailed unpaired Welch's *t*-test was performed (n = 3 independent experiments).
(E) Overlayed fluorescent speckle image of HaloTag-actin and fluorescence image of Lifeact-EGFP at the leading edge of a dendritic cell on laminin-coated dishes under agarose in the presence of 200 ng/mL CCL19. See Video S7. Time-lapse montages of the indicated rectangular region at 2 sec intervals are shown to the right panel. Magenta and green dashed lines indicate HaloTag-actin retrograde flow and F-actin extension, respectively. The actin polymerization rate (blue double-headed arrow) was calculated as the sum of the F-actin retrograde flow and extension rates. Scale bar: 10 μm (in the inset, 2 μm).
(F, G) Analyses of actin polymerization rate (F) and F-actin flow speed (G) in dendritic cells stimulated by 20 ng/mL or 200 ng/mL CCL19. One-way ANOVA with Turkey's post hoc test was performed for multiple comparisons. WT + 20 ng/mL CCL19, n = 14 cells; WT + 200 ng/mL CCL19, n = 14 cells; KO + 20 ng/mL CCL19, n = 14 cells; KO + 200 ng/mL CCL19, n = 14 cells.
(H) Schema of CCL19-induced dual enhancement of shootin1b-mediated adhesion-clutch and actin polymerization.
Data represent means ± SEM; *, $p < 0.05$; **, $p < 0.02$; ***, $p < 0.01$; ns, not significant.

Figure 4. CCL19 gradient induces asymmetric shootin1b activation to drive chemotaxis

(A, B) A gradient of CCL19 was applied to dendritic cells cultured in a mixture of collagen gel and Matrigel (left panel, A). One hour after gradient application, time-lapse phase-contrast/fluorescence images of WT (A) and shootin1b KO (B) dendritic cells expressing EGFP were obtained. Nuclei were also visualized by Hoechst to accurately trace the trajectories of cell migrations (shown in right panels and Video S8). The pictures show representative images from the time-lapse series taken every 1 min for 90 min. The

1390 tracing lines (magenta) indicate dendritic cell migration for 90 min. Scale bar: 50 μm.
1391 The right panels depict trajectories of dendritic cell migrations. The initial cell positions
1392 are normalized at x = 0 μm and y = 0 μm.
1393 (C) Scheme of chemotaxis index. Chemotaxis index was calculated as the ratio of the
1394 straight distance toward the CCL19 source (*S*) to the total distance (*T*) by tracing the
1395 migration trajectories in (A, B).
1396 (D, E) Analyses of migration speed (D) and chemotaxis index (E) of WT and shootin1b
1397 KO dendritic cells expressing flag-GST (control flag-tagged protein), and KO cells
1398 expressing flag-shootin1b-WT (H), flag-shootin1b-AA (I) and flag-shootin1b-DD (J)
1399 under the CCL19 gradient. For multiple comparison, one-way ANOVA with Turkey's
1400 post hoc test was performed. WT, n = 72 cells; KO, n = 65 cells; KO + flag-shootin1b-
1401 WT, n = 73 cells; KO + flag-shootin1b-DD, n = 72 cells; KO + flag-shootin1b-AA, n =
1402 64 cells. See Video S8.
1403 (F) Dendritic cells were transfected with myc-shootin1b to visualize shootin1b. After the
1404 stimulation by CCL19 gradients for 30 min, they were fixed and immunolabeled with
1405 anti-myc and anti-pSer249 shootin1 antibodies. Fluorescence images show the detected
1406 phosphorylated shootin1b and shootin1b in a dendritic cell. White dashed lines indicate
1407 the boundary of a dendritic cell and the center line that separates the high side (CCL19
1408 source side) and low side. Scale bar: 10 μm.
1409 (G) Quantitative data for shootin1b activation (phospho-shootin1b/shootin1b) in the
1410 CCL19 source side (high side) and low side of dendritic cells. Two-tailed Mann–Whitney
1411 *U*-test for phospho-shootin1b/total shootin1b between the high side and low side (n = 30
1412 cells).
1413 (H, I, J) Migration trajectories of shootin1b KO cells expressing flag-shootin1b-WT (H),
1414 flag-shootin1b-AA (I) and flag-shootin1b-DD (J) stimulated by the CCL19 gradient.
1415 Data represent means ± SEM; *, $p < 0.05$; **, $p < 0.02$; ***, $p < 0.01$; ns, not significant.
1416
1417 **Figure 5. Matrigel-dependent dendritic cell chemotaxis and Shootin1b mediates**
1418 **talin-independent chemotaxis *in vitro* and chemotaxis *in vivo***
1419 (A) Dendritic cells were cultured in a mixture of collagen gel and Matrigel, that contains
1420 laminin, (Matrigel +) or without Matrigel (Matrigel -). One hour after application of the
1421 CCL19 gradient, time-lapse phase-contrast/fluorescence images of dendritic cells were
1422 obtained. Nuclei were also visualized by Hoechst to accurately trace the trajectories of
1423 cell migrations. The pictures show representative images from the time-lapse series taken
1424 every 1 min for 90 min. Tracing line (magenta) indicate dendritic cell migration for 90
1425 min. Scale bar: 50 μm.

1426 (B, C) Analyses of the migration speed (B) and chemotaxis index (C) of dendritic cells in
1427 (A). Two-tailed unpaired Student's *t*-test was performed (Matrigel +, n = 89 cells;
1428 Matrigel –, n = 91 cells).
1429 (D) Dendritic cells expressing control RNAi or talin1 RNAi were cultured in a mixture
1430 of collagen gel and Matrigel. One hour after application of the CCL19 gradient, time-
1431 lapse phase-contrast/fluorescence images of dendritic cells were obtained. Nuclei were
1432 also visualized by Hoechst to trace the cell migrations (see also Video S9). Tracing line
1433 indicate dendritic cell migration for 90 min. Scale bar: 50 μm.
1434 (E, F) Analyses of migration speed (E) and chemotaxis index (F) of WT and shootin1b
1435 KO dendritic cells expressing control RNAi or talin1 RNAi vector in (D). One-way
1436 ANOVA with Turkey's post hoc test was performed for multiple comparisons. WT +
1437 control RNAi, n = 79 cells; KO + control RNAi, n = 65 cells; WT + talin1 RNAi, n = 68
1438 cells; KO + talin1 RNAi, n = 67 cells.
1439 (G) Scheme of the *in vivo* dendritic cell migration assay. WT and shootin1b KO dendritic
1440 cells were labeled by CMTPX (red) and CMFDA (green), respectively, and were mixed
1441 in a 1:1 ratio in suspension. The suspension was injected into the foot pad. Twenty-four
1442 hours after the injection, the popliteal lymph nodes were removed and the cells that
1443 arrived in the lymph nodes were analyzed (H).
1444 (H) Fluorescence images of WT (magenta) and shootin1b KO (green) cells migrated into
1445 a lymph node. The lymph node was visualized with anti-pan-laminin antibody. B, B-cell
1446 follicles; T, T-cell cortex. Scale bar: 200 μm.
1447 (I) Analyses of the ratio of the number of WT and shootin1b KO dendritic cells migrated
1448 into the lymph nodes. Two-tailed unpaired Student's *t*-test was performed (n = 3
1449 independent experiments and 3 lymph nodes).
1450 Data represent means ± SEM; *, $p < 0.05$; **, $p < 0.02$; ***, $p < 0.01$; ns, not significant.
1451
1452 **Figure 6. Shootin1b mediates weak adhesion-clutch at the leading edge of**
1453 **glioblastoma cells**
1454 (A) Immunoblot analysis of mouse astrocytes, human astrocytes, and glioblastoma cells
1455 derived from a human patient (KNBTG-8) with anti-shootin1b antibody. Actin was used
1456 as a loading control.
1457 (B) Fluorescence images of a human glioblastoma cell co-stained with anti-shootin1b
1458 antibody and phalloidin-Alexa 555 for F-actin. An enlarged view of the rectangular region
1459 is shown to the right. Arrowheads indicate shootin1b co-localization with F-actins at the
1460 tip of the tumor microtube[50,51]. The images were obtained by STED microscopy. Scale
1461 bar: 10 μm (in the inset, 2 μm).

1462 (C) Human astrocytes and human glioblastoma cells were cultured in Matrigel, and time-
1463 lapse phase-contrast images were obtained. The pictures show representative images from
1464 the time-lapse series taken every 10 min for 8 hours. Scale bar: 30 μm. See Video S11.
1465 (D) Analysis of the migration speeds of human astrocytes and human glioblastoma cells
1466 in (C). Two-tailed unpaired Welch's *t*-test was performed (human astrocytes, n = 20;
1467 human glioblastoma cells, n = 24 cells).
1468 (E) Fluorescent speckle images of HaloTag-actin at the tip of the tumor microtube of a
1469 glioblastoma cell expressing control RNAi vector on a laminin-coated dish. The
1470 expression of control RNAi or shootin1b RNAi vector was detected by EGFP. See Video
1471 S12. Time-lapse montages of the indicated rectangular regions at 5 sec intervals are
1472 shown to the right. Yellow dashed lines indicate HaloTag-actin retrograde flow. Scale bar:
1473 10 μm (in the inset, 2 μm).
1474 (F) Analyses of F-actin flow speed. Two-tailed unpaired Welch's *t*-test was performed
1475 (control RNAi, 21 speckles from 19 cells; shootin1b RNAi, 19 speckles from 14 cells).
1476 (G, H) Overlayed DIC and fluorescence images showing the tip of the tumor microtube
1477 of glioblastoma cells expressing control RNAi (G) and shootin1b RNAi (H) cultured on
1478 laminin-coated polyacrylamide gels embedded with 200-nm fluorescent beads. See Video
1479 S13. The pictures show representative images from the time-lapse series taken every 3
1480 sec for 180 sec. The original and displaced positions of the beads in polyacrylamide gel
1481 are indicated by green and red colors, respectively. The tip of the tumor microtube were
1482 visualized by EGFP (blue color); dashed lines indicate the boundaries of the cells. The
1483 kymographs (right panels) along the axis of bead displacement (white dashed arrows) at
1484 indicated areas 1 and 2 show the movement of beads recorded by every 3 sec. The beads
1485 in area 2 are reference bead. Scale bar: 5 μm (in the inset, 1 μm).
1486 (I) Analyses of the magnitude of the traction force under the tip of the tumor microtube
1487 of glioblastoma cells expressing control RNAi or shootin1b RNAi vector. Two-tailed
1488 unpaired Welch's *t*-test was performed (control RNAi, n = 17 cells; shootin1b RNAi, n =
1489 15 cells).
1490 Data represent means ± SEM; *, $p < 0.05$; ***, $p < 0.01$.
1491
1492 **Figure 7. Aberrant activity of shootin1b promotes glioblastoma cell motility**
1493 (A, B, D, E) Human glioblastoma cells were cultured in Matrigel, and time-lapse phase-
1494 contrast images of the cells expressing control RNAi (A) or shootin1b RNAi (B) vector
1495 and overexpressing EGFP (control) (D) or EGFP-shootin1-DN (E) were obtained. The
1496 expression of control RNAi or shootin1b RNAi vector was detected by EGFP (left panel).

The pictures show representative images from the time-lapse series taken every 10 min for 8 hours. See Video S11. Scale bar: 30 μm.

(C, F) Analyses of migration speed of human glioblastoma cells expressing control RNAi or shootin1b RNAi vector (C) and overexpressing EGFP or EGFP-shootin1-DN (F). Two-tailed Mann-Whitney *U*-test was performed for the migration speed of cells expressing control RNAi or shootin1b RNAi (C). Two-tailed Mann-Whitney *U*-test was performed for the migration speed of cells overexpressing EGFP or EGFP-shootin1-DN (F) (control RNAi, n = 44 cells; shootin1b RNAi, n = 48 cells; EGFP, n = 51 cells; EGFP-shootin1-DN, n = 22 cells).

(G) Scheme of the glioblastoma invasion assay. Glioblastoma cells were infected with lentiviruses carrying shScramble-mCherry (control RNAi, red) or shShootin1b-EGFP (shootin1b RNAi, green). Tumor spheroids (T) were formed by mixing control RNAi cells (red) and shootin1b RNAi cells (green) in a 1:1 ratio, and co-cultured with the brain cortex organoids (Cx) derived from human iPS cells. The migration distance of the control RNAi cells and shootin1b RNAi cells invaded into the organoids (H) was then analyzed.

(H) Fluorescence images of control RNAi cells (magenta) and shootin1b RNAi cells (green) invaded into a brain cortex organoid (Cx) from a tumor spheroid (T). Enlarged images in the rectangles are shown to the right. Scale bar: 50 μm (in the inset, 20 μm).

(I) Migration distance of the control RNAi cells and shootin1b RNAi cells invaded into the organoids The number of cells was expressed as the percentage of cells in the migration distance range of 0~100 μm, 100~200 μm and 200~300 μm. Two-tailed unpaired Student's *t*-test for the ratio at the range of 0~100 μm. Two-tailed unpaired Welch's *t*-test for the for the ratio at the range of 100~200 μm. Two-tailed unpaired Welch's *t*-test for the for the ratio at the range of 200~300 μm. n = 5 brain cortex organoids.

(J) Weak and strong adhesion-clutch model: adhesion-clutch can mediate both cell motility and immobilization depending on the force amplitude. Weak adhesion-clutch is well-suited for rapid cell migration, without forming strong adhesions that impede cell motility. As transmission of large forces requires strong adhesion, strong adhesion-clutch can immobilize cells against mechanical stress.

Data represent means ± SEM; ***, $p < 0.01$; ns, not significant.

Figure 1 Baba et al.

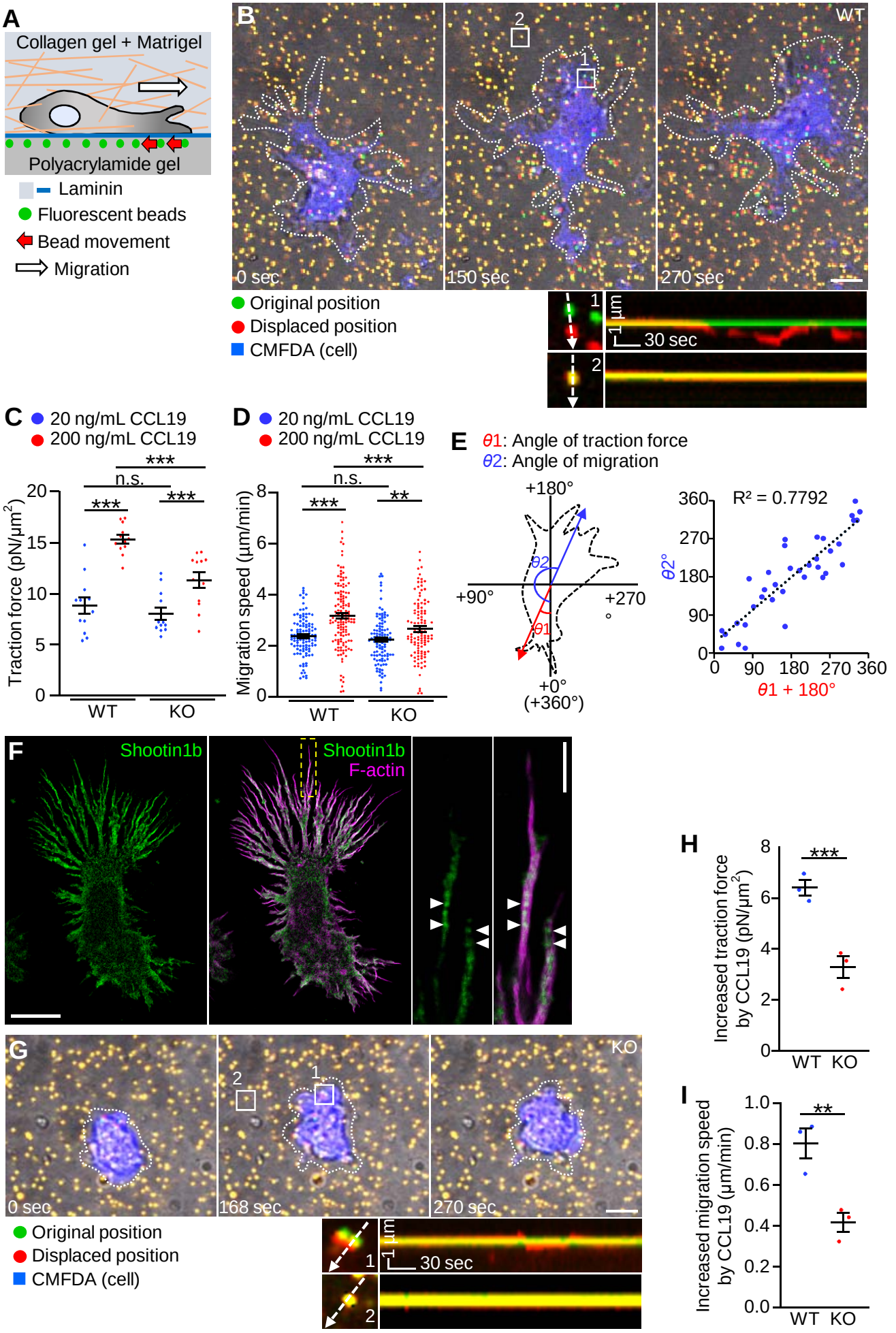

Figure 2 Baba et al.

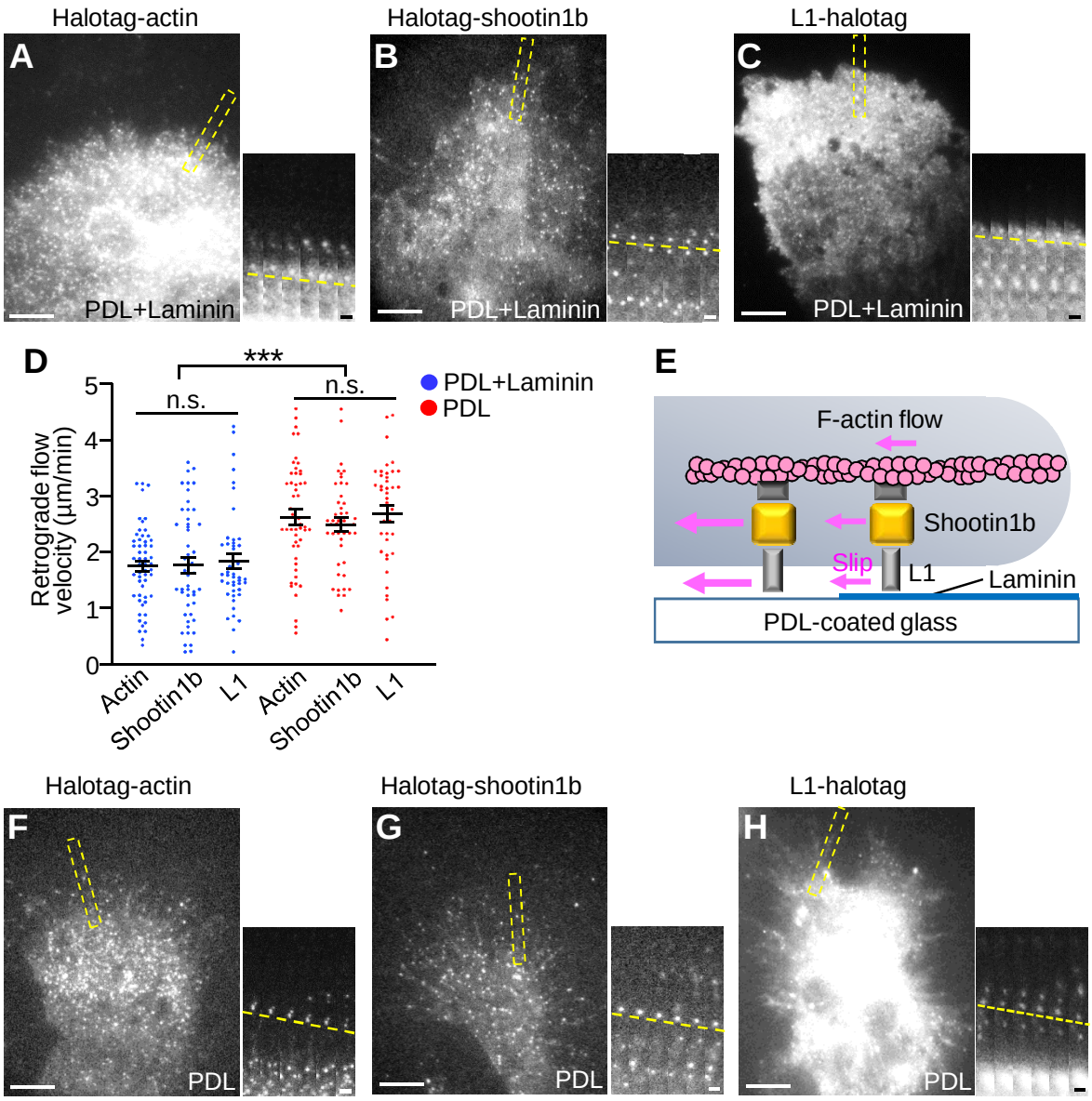

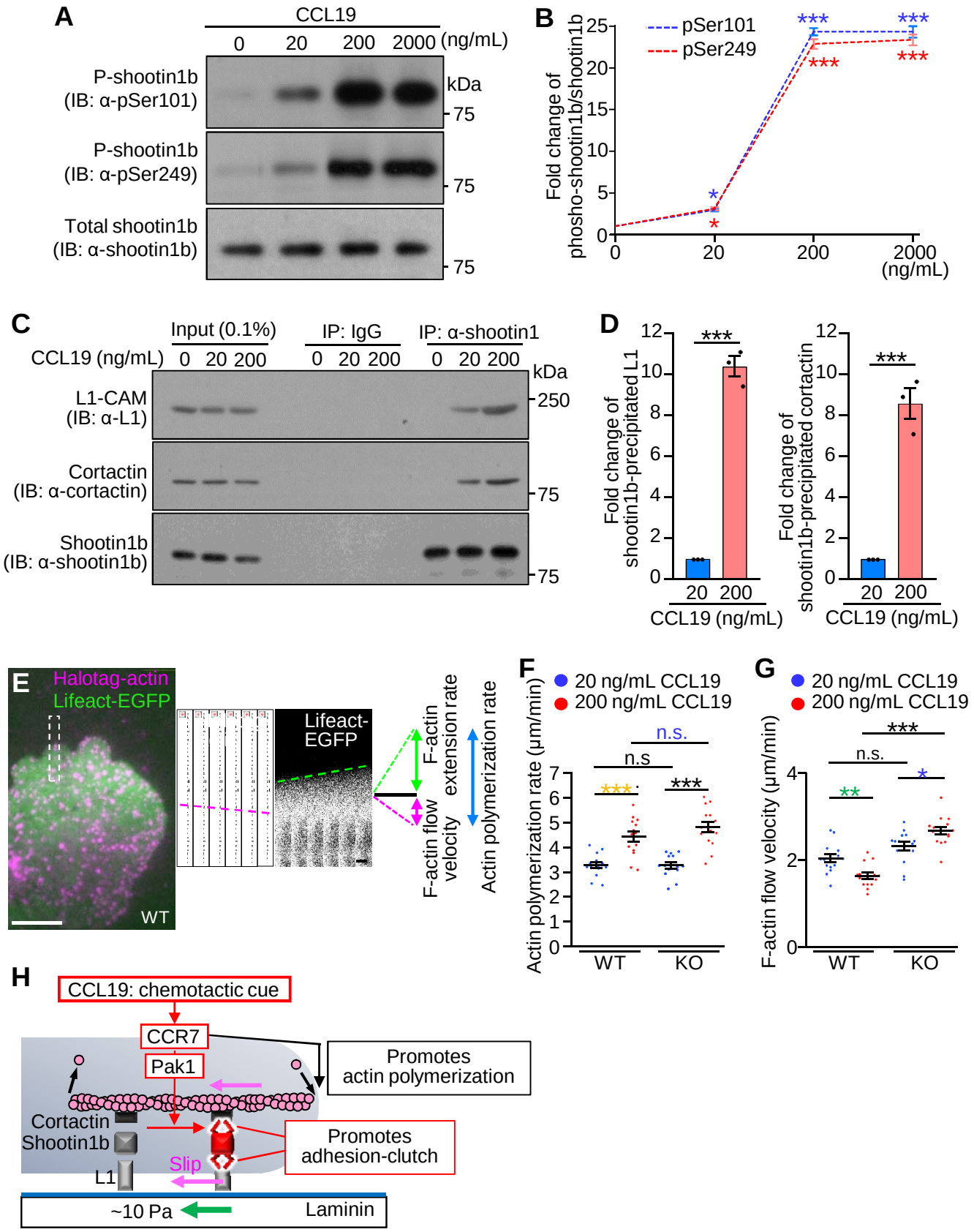
A
CCL19
0 20 200 2000 (ng/mL)
P-shootin1b (IB: α-pSer101)
P-shootin1b (IB: α-pSer249)
Total shootin1b (IB: α-shootin1b)
kDa
75
B
pSer101
pSer249
Fold change of phosho-shootin1b/shootin1b
(ng/mL)
C
Input (0.1%)
IP: IgG
IP: α-shootin1
CCL19 (ng/mL)
L1-CAM (IB: α-L1)
Cortactin (IB: α-cortactin)
Shootin1b (IB: α-shootin1b)
250
D
Fold change of shootin1b-precipitated L1
Fold change of shootin1b-precipitated cortactin
CCL19 (ng/mL)
E
Halotag-actin
Lifeact-EGFP
WT
Lifeact-EGFP
F-actin extension rate
F-actin flow velocity
Actin polymerization rate
F
20 ng/mL CCL19
200 ng/mL CCL19
Actin polymerization rate (μm/min)
n.s.
n.s
WT
KO
G
F-actin flow velocity (μm/min)
H
CCL19: chemotactic cue
CCR7
Pak1
Promotes actin polymerization
Cortactin
Shootin1b
L1
Slip
Promotes adhesion-clutch
~10 Pa
Laminin

Figure 4 Baba et al.

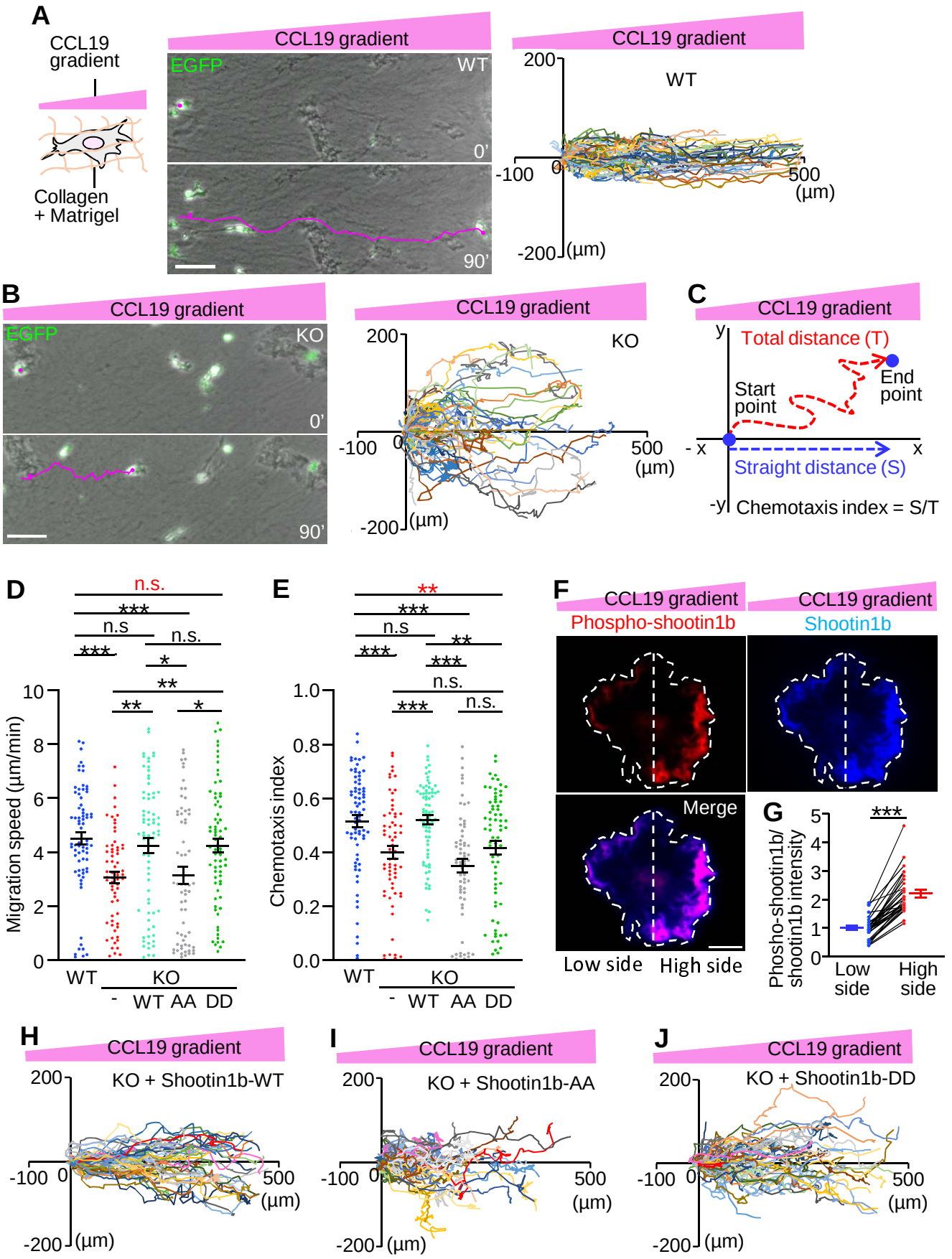

Figure 5 Baba et al.

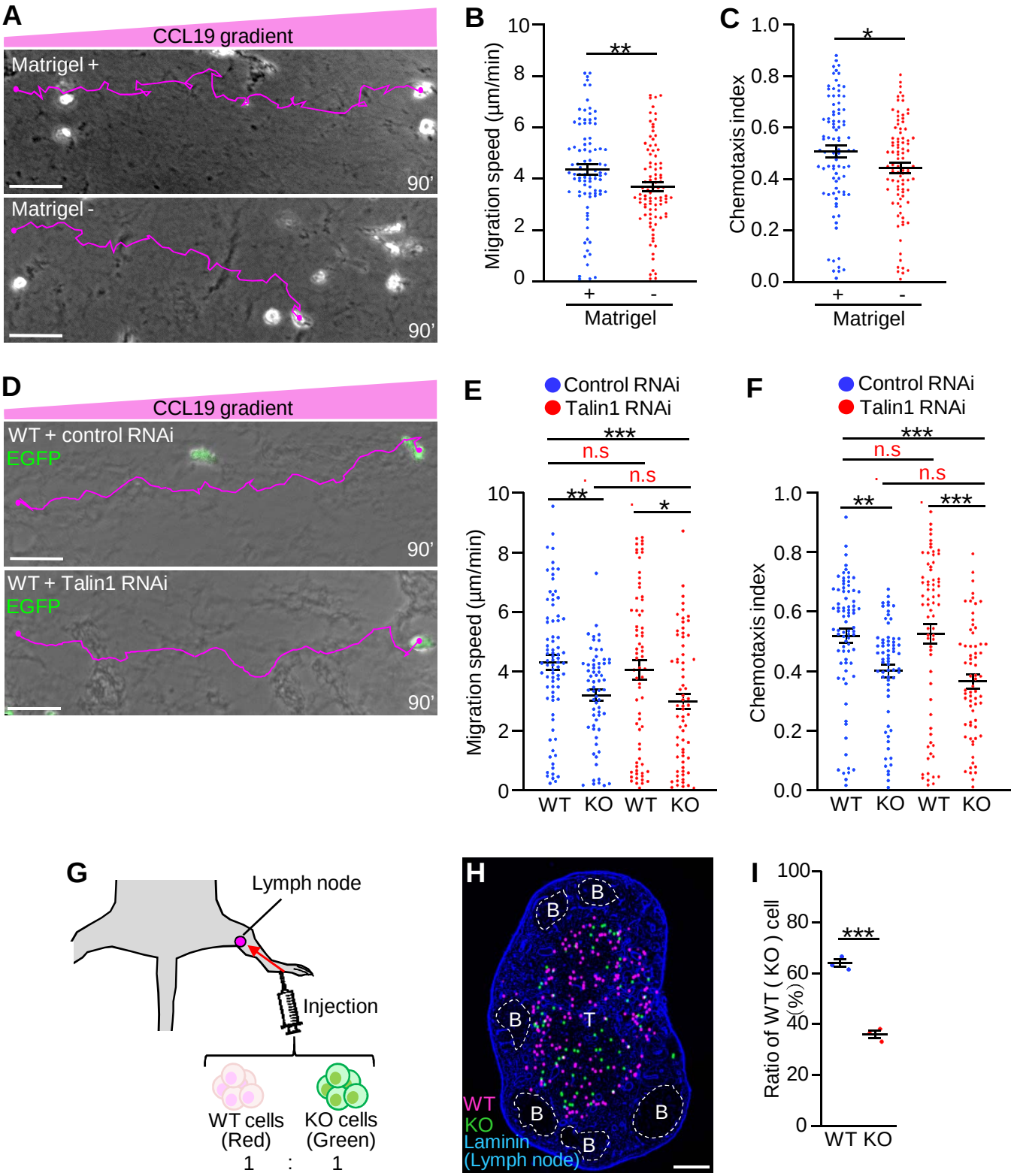

Figure 6 Baba et al.

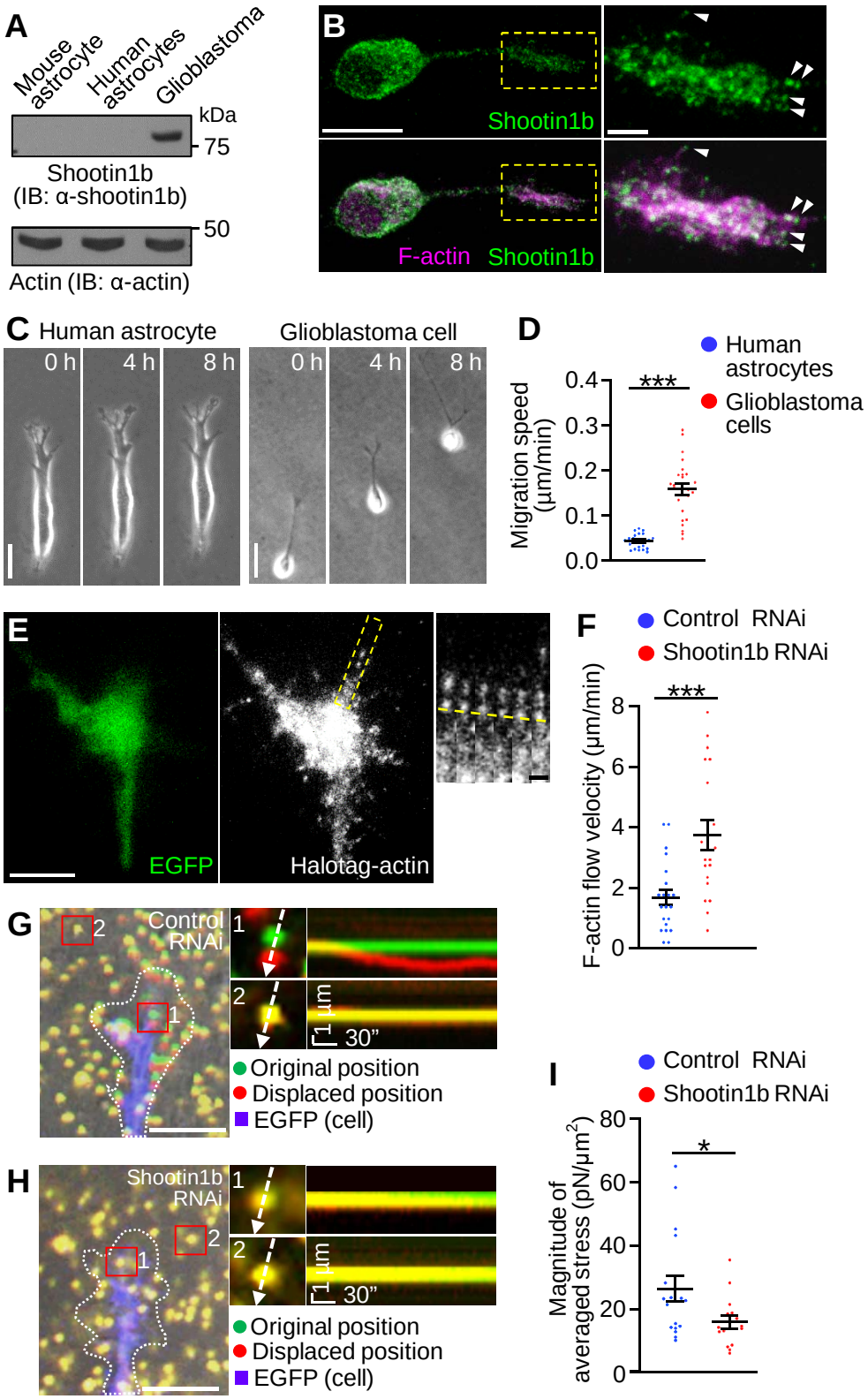

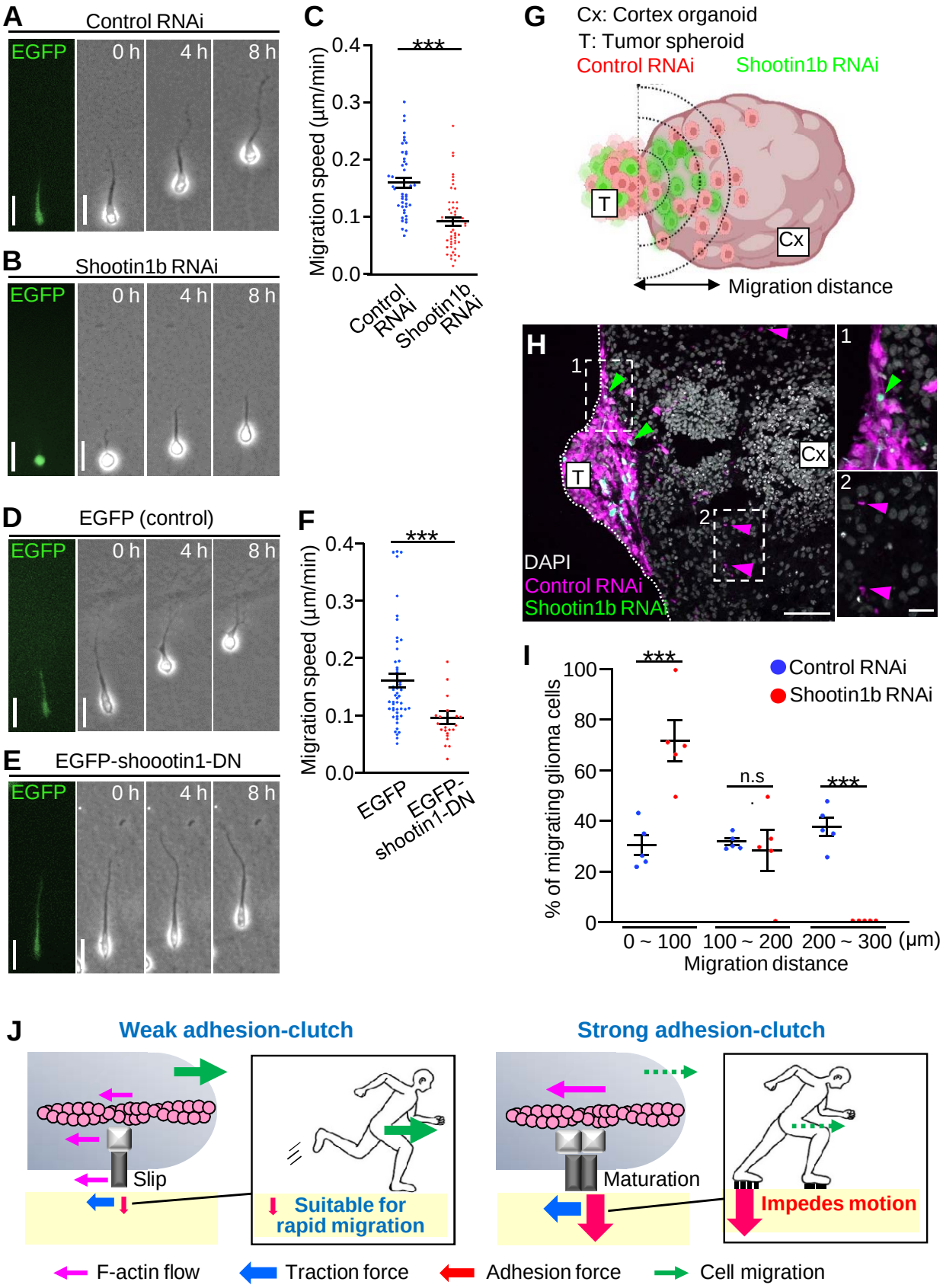
A
Control RNAi
EGFP
0 h
4 h
8 h
B
Shootin1b RNAi
C
Migration speed (μm/min)
0.4
0.3
0.2
0.1
0.0
***
Control RNAi
Shootin1b RNAi
D
EGFP (control)
E
EGFP-shoootin1-DN
F
EGFP
EGFP-shootin1-DN
G
Cx: Cortex organoid
T: Tumor spheroid
Control RNAi
Shootin1b RNAi
T
Cx
Migration distance
H
1
2
DAPI
Control RNAi
Shootin1b RNAi
I
% of migrating glioma cells
100
80
60
40
20
0
n.s
0 ~ 100
100 ~ 200
200 ~ 300 (μm)
Migration distance
J
Weak adhesion-clutch
Slip
Suitable for rapid migration
Strong adhesion-clutch
Maturation
Impedes motion
F-actin flow
Traction force
Adhesion force
Cell migration